

Alleviation of liver fibrosis by inhibiting a non-canonical ATF4-regulated enhancer program in hepatic stellate cells

Received: 25 November 2023

Accepted: 20 December 2024

Published online: 09 January 2025



Li-Xian Yang^{1,2,3,12}, Chuangye Qi^{4,12}, Si Lu^{1,5,12}, Xiang-Shi Ye^{1,2,12}, Parnaz Merikhian^{4,6}, Du-Yu Zhang^{1,2}, Tao Yao^{1,2,7}, Jiang-Sha Zhao^{1,2}, Ying Wu^{7,8}, Yongshi Jia³, Bo Shan^{1,2}, Jinghai Chen⁹, Xiaozhou Mou¹⁰, Jia You¹¹✉, Wenbo Li^{4,6}✉ & Yu-Xiong Feng^{1,2}✉

Liver fibrosis is a critical liver disease that can progress to more severe manifestations, such as cirrhosis, yet no effective targeted therapies are available. Here, we identify that ATF4, a master transcription factor in ER stress response, promotes liver fibrosis by facilitating a stress response-independent epigenetic program in hepatic stellate cells (HSCs). Unlike its canonical role in regulating UPR genes during ER stress, ATF4 activates epithelial-mesenchymal transition (EMT) gene transcription under fibrogenic conditions. HSC-specific depletion of ATF4 suppresses liver fibrosis in vivo. Mechanistically, TGFβ resets ATF4 to orchestrate a unique enhancer program for the transcriptional activation of pro-fibrotic EMT genes. Analysis of human data confirms a strong correlation between HSC ATF4 expression and liver fibrosis progression. Importantly, a small molecule inhibitor targeting ATF4 translation effectively mitigates liver fibrosis. Together, our findings identify a mechanism promoting liver fibrosis and reveal new opportunities for treating this otherwise non-targetable disease.

Liver fibrosis is a common pathological outcome of liver injuries of various etiologies, with excessive accumulation of extracellular matrix (ECM) being the most important hallmark¹. Hepatic metabolic syndromes (e.g., nonalcoholic fatty liver disease (NAFLD) and nonalcoholic steatohepatitis (NASH)), alcohol abuse, and viral hepatitis are the

leading causes of liver fibrosis, all of which damage hepatocytes and result in acute or chronic liver injuries^{2–4}. In response to these injuries, a massive inflammatory response arises in the liver to clear damaged hepatocytes⁵. Such response activates liver resident fibrogenic cell populations to synthesize and secrete ECM proteins, the progression

¹Zhejiang Key Laboratory of Pancreatic Disease, The First Affiliated Hospital, Zhejiang Key Laboratory of Frontier Medical Research on Cancer Metabolism, Institute of Translational Medicine, Zhejiang University School of Medicine, Hangzhou, China. ²Institute of Fundamental and Transdisciplinary Research, Cancer Center, Zhejiang University, Hangzhou, China. ³Cancer Center, Department of Radiation Oncology, Zhejiang Provincial People's Hospital, Affiliated People's Hospital, Hangzhou Medical College, Hangzhou, China. ⁴Department of Biochemistry and Molecular Biology, McGovern Medical School, University of Texas Health Science Center, Houston, TX, USA. ⁵Department of Head and Neck Surgery, Sir Run-Run Shaw Hospital, Zhejiang University School of Medicine, Hangzhou, China. ⁶Graduate School of Biomedical Sciences, University of Texas MD Anderson Cancer Center and UTHealth, Houston, TX, USA. ⁷College of Life Sciences, Zhejiang Chinese Medical University, Hangzhou, China. ⁸Zhejiang Academy of Traditional Chinese Medicine, Tongde Hospital of Zhejiang Province, Hangzhou, China. ⁹Department of Cardiology of Second Affiliated Hospital, State Key Laboratory of Transvascular Implantation Devices, Heart Regeneration and Repair Key Laboratory of Zhejiang Province, Institute of Translational Medicine, Zhejiang University School of Medicine, Hangzhou, China. ¹⁰Clinical Research Institute, Zhejiang Provincial People's Hospital, People's Hospital of Hangzhou Medical College, Hangzhou, China. ¹¹School of Life Sciences, Westlake University, Hangzhou, China. ¹²These authors contributed equally: Li-Xian Yang, Chuangye Qi, Si Lu, Xiang-Shi Ye.

✉ e-mail: youjia@westlake.edu.cn; wenbo.li@uth.tmc.edu; yxfeng@zju.edu.cn

of which will lead to liver fibrosis and can further deteriorate into cirrhosis or primary hepatocellular carcinoma (HCC)⁶. In contrast to the stages of cirrhosis and HCC, liver fibrosis is considered reversible since the hepatic architecture remains relatively normal and the liver preserves compensatory functions². Therefore, it is clinically crucial to intervene in the progression of liver fibrosis prior to late-stage liver diseases. However, due to the lack of targeted therapies that can suppress or reverse liver fibrosis, eliminating the cause of hepatic injuries remains the most effective therapy to date⁷. It is important to develop new strategies to target liver fibrosis, which requires an in-depth understanding of the mechanisms of this disease.

Hepatic stellate cells (HSCs) are a resident non-parenchymal liver cell population, which is the primary fibrogenic cell type in response to liver injury⁸. In a normal liver, HSCs maintain a non-proliferative, quiescent cell state⁹. Following liver injury, HSCs become activated, transdifferentiating from lipid-storing cells to myofibroblasts (or myofibroblast-like cells), which are proliferative, contractile, inflammatory, and most importantly, characterized by enhanced ECM production¹⁰. While a panoply of intracellular events and signaling pathways, including oxidative stress, autophagy, and metabolic reprogramming, can contribute to or mediate HSC activation in response to extracellular triggers (e.g., TGF β , PDGF, CTGF, Hedgehogs, etc.), the master program that governs HSC activation remains unclear¹¹.

It has been proposed that epithelial-mesenchymal transition (EMT) plays an important role in tissue fibrosis of many origins, including lung, kidney, and liver^{12,13}. Intriguingly, EMT and HSC activation share some common features: both of them are transdifferentiation processes in that EMT allows epithelial cells to depart their original characteristics and obtain mesenchymal phenotypes^{14,15}, while activation of HSCs is essentially transdifferentiation of the quiescent, perisinusoidal cells into mesenchymally differentiated myofibroblasts. Additionally, the hallmark consequence of HSC activation is the accumulation of ECM proteins, which is exactly the signature product of EMT¹¹. Despite these commonalities, the molecular interplay between HSC activation and EMT remains incompletely understood¹⁶. It is crucial to investigate the underlying mechanisms of how EMT regulates HSC activation, which may reveal new therapeutic opportunities.

Cancer cells that undergo an EMT (hereafter referred to as EMT cancer cells) exhibit increased synthesis and secretion of ECM proteins, a phenomenon similar to activated HSCs. To cope with the augmented burden of ECM secretome, EMT cancer cells activate the PERK branch of the unfolded protein response (UPR) pathway¹⁷. Upon activation, PERK phosphorylates eIF2 α , which then increases the translation of ATF4 either to promote cell survival by regulating protein synthesis and folding or to induce cell apoptosis when necessary¹⁸. In addition to its role in ER homeostasis, activation of the PERK-eIF2 α -ATF4 pathway is required for cancer metastasis and drug resistance, the two hallmark features of EMT cancer cells¹⁷. However, it has not been explored if the PERK pathway can control the EMT program in the non-cancer setting to govern cell transdifferentiation and cell fate.

Cell fate determination is dictated by master transcription factors (TFs)¹⁹. ATF4 is the transcription factor that mediates the major cellular events in the PERK pathway. Indeed, ATF4 executes the PERK program by regulating stress response gene expression in response to various stress conditions, including ER stress, nutrient deprivation, and viral infection^{20,21}. Evidence has implicated the role of ATF4 in EMT. For example, ATF4 is upregulated when cancer cells are under nutrition deprivation and it is required for the expression of essential pro-EMT TFs such as Slug²². Similarly, ATF4 promotes neural crest cell migration, a process that requires EMT induction²³.

Here, we systemically examined the function of ATF4 in EMT biology in a poorly explored non-cancer setting—HSC activation. We found that in response to cellular signals that trigger EMT, ATF4

determines cell fate in both epithelial cells and HSCs by directly impacting the epigenome. Genetic deletion of *Atf4* in mouse HSCs, as well as chemical inhibition of ATF4 translation, blocks HSC activation and inhibits the progression of liver fibrosis. Our findings elucidated a critical role of ATF4 in cell fate decision and revealed a target for treating liver fibrosis.

Results

ATF4 governs gene expression in a signal-dependent manner

In response to cellular stress, the classical role of ATF4 is to activate the transcription program of stress response genes²¹. We wondered if ATF4 may drive distinct gene transcription programs in response to non-stress alternative stimuli. To test this, we used HMLE, an immortalized epithelial cell line known to be responsive to ER stressors and EMT-inducing transcription factors (EMT-TFs)¹⁷. Both control and ATF4-knockdown HMLE cells were treated with various conditions followed by gene expression profiling analysis. Stress conditions were introduced by thapsigargin (Tg) treatment or amino acid deprivation (AA-Dep), while EMT was induced by overexpression of Twist (Twist-OE), a classical EMT-TF²⁴. As expected, the expression of stress response genes (including *ASNS*, *DDIT3*, and *SLC7A11*) was strongly induced by ER stress or AA-Dep and was effectively suppressed when ATF4 was downregulated (Supplementary Fig. 1a)²⁵. However, when we compared the most significantly changed genes upon ATF4-knockdown across different conditions, we found that ATF4-regulated genes upon non-stress Twist-OE were markedly different from those under stress (Twist-OE vs Tg; Fig. 1a). Enrichment analyses confirmed that ATF4 mainly regulated stress response pathways (e.g., genesets of “Amino acid deprivation” and “Unfolded protein response”) under stress (Fig. 1b and Supplementary Fig. 1b). In contrast, the most significant pathway regulated by ATF4 upon Twist-OE was the EMT pathway (Fig. 1c). Indeed, a great many mesenchymal genes, such as collagens, *FNI*, and *VIM*, were downregulated upon knockdown of ATF4 (Supplementary Fig. 1c). These findings suggest that ATF4 regulates distinctive context-specific gene transcriptional programs in response to stress or non-stress signals.

In addition to the overexpression of EMT-TFs, the EMT program can be triggered by extracellular factors, such as TGF β , which is the driving signal of HSC activation²⁶. Using LX-2, an immortalized human HSC line, we further studied the context-specific role of ATF4 in regulating gene expression (Fig. 1d)²⁷. Like in HMLE, in LX-2 cells, ATF4 mainly controlled the expression of stress response genes when cells were challenged with Tg or AA-Dep (Fig. 1e and Supplementary Fig. 1d). However, under the treatment of TGF β , the genes most significantly regulated by ATF4 belonged to the EMT pathway (Fig. 1f and Supplementary Fig. 1e). This phenomenon was consistent with ATF4's role in HMLE in regulating Twist-induced EMT genes expression. These results together indicate that ATF4-driven transcriptional landscapes can be reprogrammed in response to different triggers. More importantly, our findings suggest that ATF4 is not only a stress-responsive transcription factor but can also play unappreciated roles in cell state transition.

ATF4 is required for the induction of EMT in epithelial cells

Reciprocal change in mesenchymal and epithelial cell state marker gene expression is a hallmark of EMT induction. In the HMLE cell model, Twist-driven (Fig. 2a, Twist was induced by 4-OHT) expression of mesenchymal markers, such as FNI, N-cadherin, Vimentin, and Slug, was dramatically reduced when ATF4 was knocked down (Fig. 2a and Supplementary Fig. 2a). In contrast, the expression of epithelial markers Claudin-1 and *CDH1* was increased (Fig. 2a and Supplementary Fig. 2a). Similar changes of cell state markers were observed if EMT was initiated by overexpressing Snail, another key pro-EMT TF (Supplementary Fig. 2b, Snail was induced by doxycycline (DOX)). Gaining mesenchymal cell

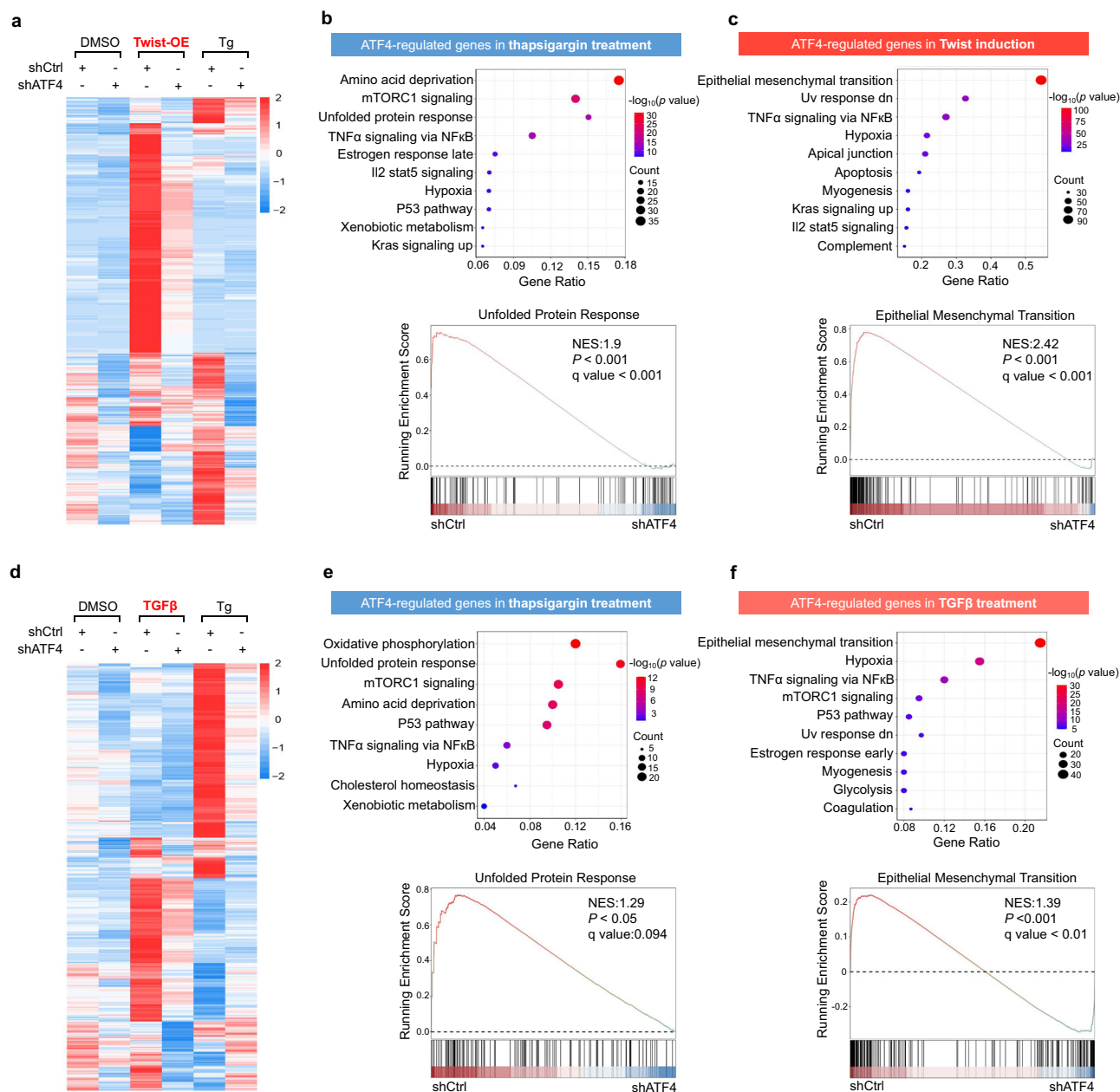


Fig. 1 | ATF4 governs gene expression in a signal-dependent manner. **a–c** RNA-seq was conducted on the HMLE cells transduced with a scramble shRNA (shCtrl) or an ATF4-targeted shRNA (shATF4) and treated with indicated conditions (Twist-OE, Twist overexpression; Tg, thapsigargin). **a** A heatmap showing the expression of genes that were downregulated by ATF4 knockdown and ranked in the top 2.5% under Twist-OE or Tg treatment, respectively. **b** GO (gene ontology) enrichment analysis for genes downregulated by ATF4 knockdown for more than 1.5-fold in Tg treatment. A list of top enriched genesets (upper panel) and a GSEA (gene set enrichment analysis) plot showing the enrichment of the unfolded protein response pathway (lower panel) were shown. Hypergeometric test was used to identify significant enrichment pathways ($P < 0.01$). The statistical significance (nominal P value) of the normalized enrichment score (NES) was generated by employing an empirical phenotype-based permutation test. **c** GO enrichment

analysis for genes downregulated by ATF4 knockdown for more than 1.5-fold when Twist was induced. A list of top enriched genesets (upper panel) and a GSEA plot showing the enrichment of the epithelial-mesenchymal transition pathway (lower panel) were shown. Hypergeometric test was used to identify significant enrichment pathways ($P < 0.01$). The statistical significance (nominal P value) of the normalized enrichment score (NES) was generated by employing an empirical phenotype-based permutation test procedure. **d–f** RNA-seq was conducted on the LX-2 cells transduced with a scramble shRNA (shCtrl) or an ATF4-targeted shRNA (shATF4) and treated with indicated conditions. Similar analyses were conducted as in (a–c). Hypergeometric distribution tests were applied for GO enrichment analysis and weighted Kolmogorov–Smirnov tests were applied for GSEA. These analyses were conducted on the average data of two biological replicates.

morphology represents an immediate outcome of EMT initiation. We found that Twist-OE in HMLE cells led to a scattering spindle morphology that reflects their transition to mesenchymal state, while ATF4 knockdown effectively abrogated this change of Twist-OE cells, and they maintained a typical epithelial cell shape (Fig. 2b and Supplementary Fig. 2c). Consistently, ATF4 knockdown repressed cell migration, another characteristic of EMT (Fig. 2c). In

addition, initiation of EMT led to the enrichment of a CD24^{lo}CD44^{hi} stem cell-like population in epithelial cells²⁸. We found that Twist-OE increased the CD24^{lo}CD44^{hi} populations in the HMLE cells, whereas ATF4 knockdown effectively blocked the enrichment of this stem cell-like population (Fig. 2d). These results demonstrate that ATF4 regulates the EMT molecular program and is required for EMT induction in epithelial cells.

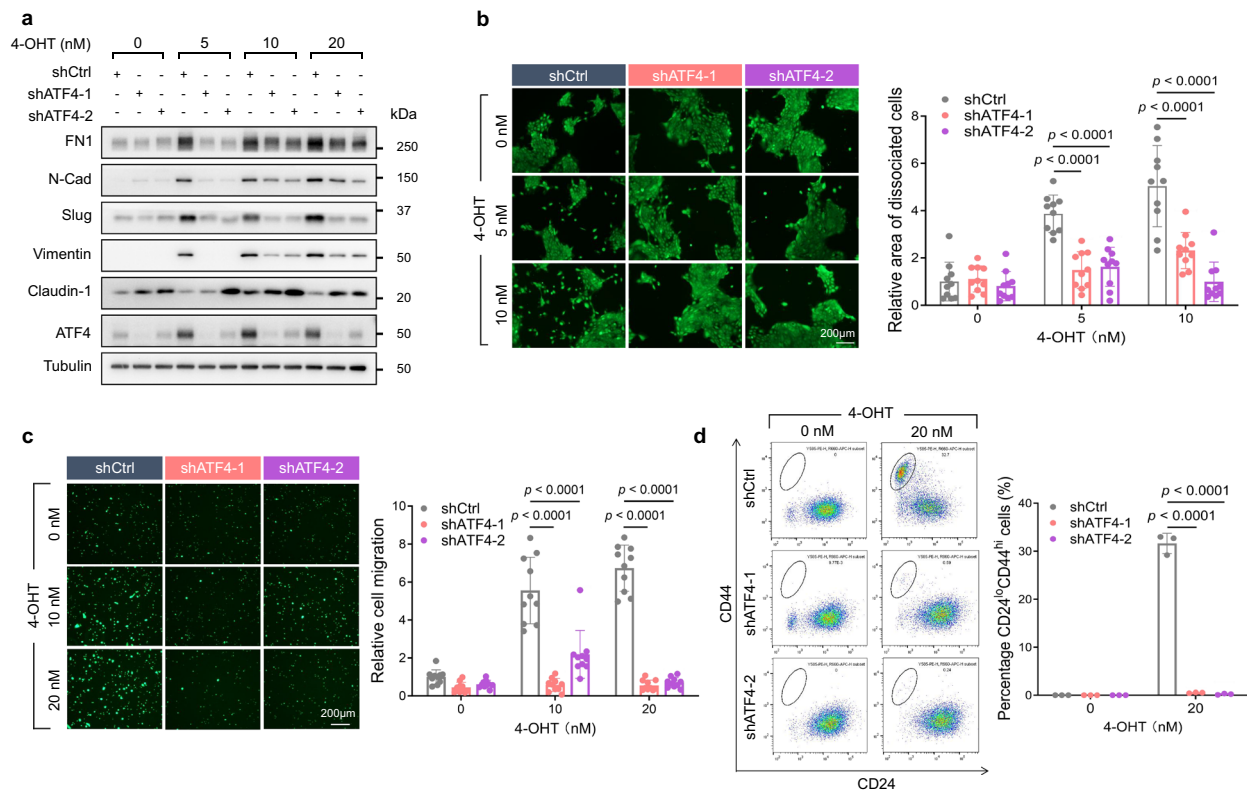


Fig. 2 | ATF4 is required for the induction of EMT in epithelial cells. The HMLE cell line was transduced with a scramble (shCtrl) or two ATF4-targeted shRNAs (shATF4-1 and shATF4-2). The EMT program of the HMLE cells was triggered by 4-hydroxytamoxifen (4-OHT)-mediated nuclear translocation of a Twist-ER fusion protein (see methods for details). **a** Western blots showing the expression of EMT marker genes in HMLE-shCtrl and HMLE-shATF4 cells treated with increasing concentrations of 4-OHT for 10 days. The experiment was repeated three times. **b** Calcein-AM staining showing the morphology of HMLE-shCtrl and HMLE-shATF4 cells treated with 4-OHT for 10 days. Representative fluorescence images (left) and quantitative analysis of dissociated cells (right) were shown ($n = 10$ images

derived from 3 biological replicates). **c** Migratory ability of HMLE-shCtrl and HMLE-shATF4 cells treated with 4-OHT was gauged by a transwell assay. Representative images of Calcein-AM labeled cells passed through transwell chambers (left) and quantitative analysis (right) were shown ($n = 10$ images derived from 3 biological replicates). **d** Representative flow cytometry plots showing the distribution of CD24^{lo}CD44^{hi} cells in HMLE-shCtrl and HMLE-shATF4 cells treated with or without 4-OHT for 10 days (left), and quantification analysis of the flow cytometry assay (right) ($n = 3$ biological replicates). Data are presented as mean \pm s.e.m and representative of at least three independent experiments. Unpaired, two-tailed Student's t tests were applied for (**b–d**). Source data are provided as a Source Data file.

ATF4 positively regulates the EMT program in HSCs and is required for HSC activation

The EMT program is also involved in the process of HSC activation, since upregulation of mesenchymal marker genes is a prominent feature of activated HSCs. While TGF β treatment increased mesenchymal marker genes expression in LX-2 cells, including FN1, N-cadherin, and Slug, ATF4 knockdown abolished such upregulation (Fig. 3a and Supplementary Fig. 2d). ISRIB, a chemical activator of eIF2B thus inhibiting the function of p-eIF2 α , can result in reduced translation of ATF4²⁹. Consistent with genetic knockdown, this small molecule also repressed the expression of TGF β -responsive genes (Fig. 3b). In contrast, overexpression of ATF4 (ATF4-OE) strongly potentiated LX-2 cells to TGF β -induced mesenchymal genes expression (Fig. 3c, d; Supplementary Fig. 2e). For instance, in the presence of ATF4-OE, only 0.5 ng/ml of TGF β could induce *SNAIL* and *FN1* expression to levels comparable to those caused by 5 ng/ml of TGF β in normal LX-2 cells (Fig. 3d).

Beyond the increase of classical mesenchymal genes, induction of α -smooth muscle actin (α -SMA) and collagen proteins represents a hallmark of HSC activation³⁰. While TGF β treatment increased the expression of α -SMA (coded by the *ACTA2* gene), ATF4 knockdown effectively blocked this induction (Fig. 3e, f). In addition to α -SMA, loss of ATF4 also repressed the expression of TGF β -induced type I collagens, markers of liver fibrosis (Fig. 3f). Conversely, ATF4-OE strongly potentiated the TGF β -driven expression of fibrotic markers (Fig. 3g). Downregulation of ATF4 translation by ISRIB effectively suppressed

the expression of α -SMA and type I collagens (Fig. 3h). Similar regulatory effects by ISRIB were observed in the PDGF-BB-triggered HSC activation model (Supplementary Fig. 2f, g). More importantly, the effect of ISRIB was completely rescued by overexpression of ATF4 in LX-2 cells, suggesting the anti-fibrotic role of ISRIB was mediated by ATF4 (Supplementary Fig. 2h, i). As a comparison, the regulatory effects of p-eIF2 α -ATF4 on the expression of ECM genes were notably less pronounced in AML12 cells, a hepatocyte cell line (Supplementary Fig. 2h, i). Together, these results indicate that ATF4 licenses HSC activation by promoting the EMT molecular program in HSCs.

HSC-specific depletion of *Atf4* alleviates liver fibrosis in vivo

HSC activation is an essential event of liver fibrosis. We next investigated if ATF4 plays a role in the pathologic progression of liver fibrosis in vivo. We established an HSC-specific *Atf4*-knockout mouse model *Lrat-Cre;Atf4^{fl/fl}* (Fig. 4a). In this model, Cre expression was driven by the *lecithin retinol acyltransferase* (*Lrat*) promoter, which assured specific knockout of the *Atf4* gene in HSCs³¹. To confirm *Atf4* depletion, we tested the expression of *Atf4* in primary HSCs isolated from the *Atf4^{fl/fl}* (WT) and the *Lrat-Cre;Atf4^{fl/fl}* (HSC-*Atf4*-KO) mice and found that the expression of *Atf4* was specifically reduced in the *Atf4*-depleted HSCs while other tissues were not affected (Supplementary Fig. 3a–e). We then applied CCl₄, a commonly used fibrotic agent, to induce liver fibrosis. After five weeks of induction, liver tissue was collected to assess fibrotic progression. In the WT animals, mesenchymal markers,

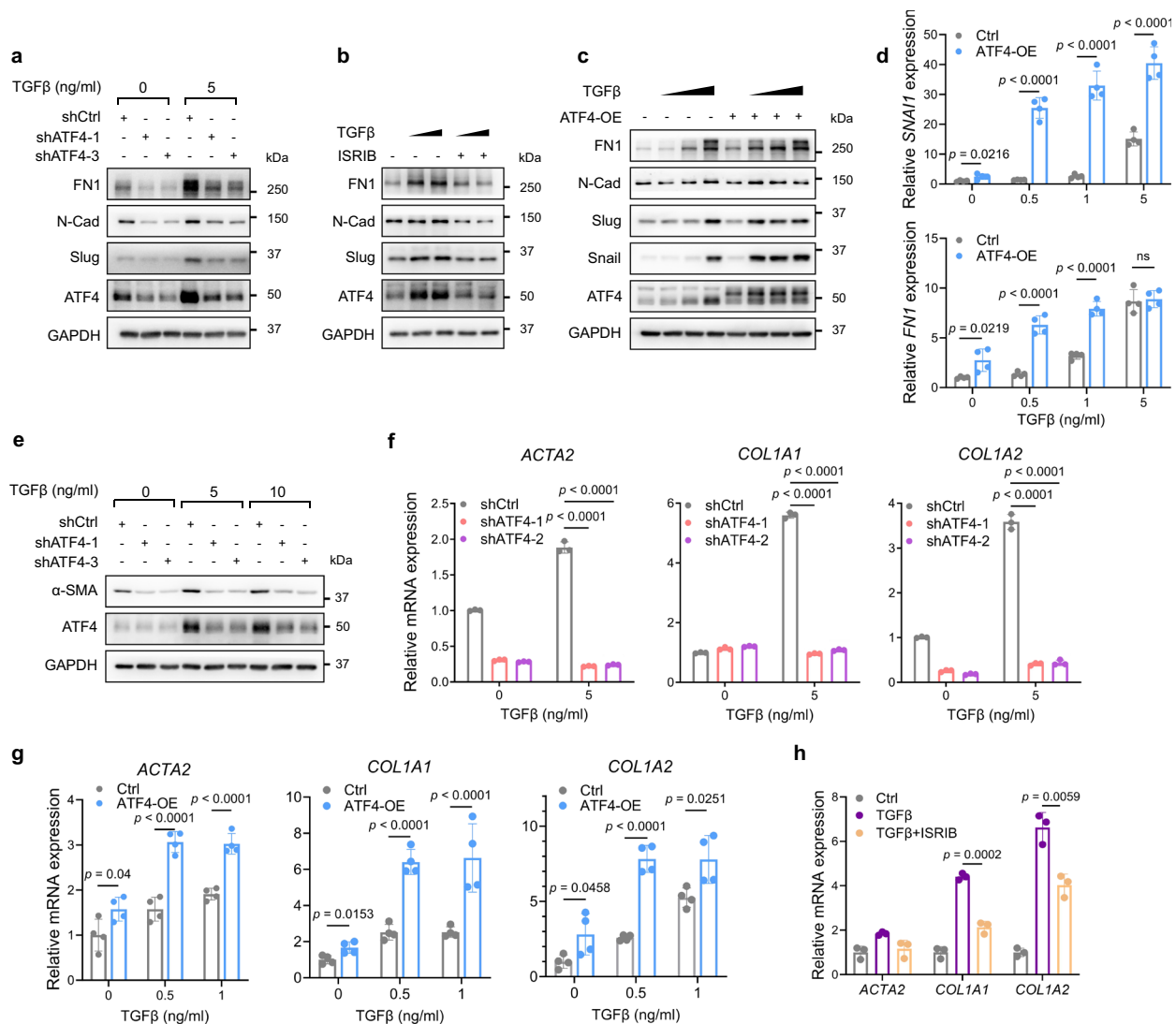


Fig. 3 | ATF4 positively regulates EMT program in HSCs and is required for HSC activation. **a** Western blots showing the expression of mesenchymal marker genes in LX-2-shCtrl and LX-2-shATF4 cells treated with or without TGFβ for 2 days. The experiment was repeated four times. **b** Western blots showing the expression of mesenchymal marker genes in LX-2 cells treated with or without ISRIB (1 mM) and TGFβ (0, 1, and 5 ng/ml). The experiment was repeated three times. **c** Western blots showing the expression of mesenchymal marker genes in LX-2 cells overexpressing ATF4 treated with or without increasing concentrations of TGFβ (0, 0.5, 1, and 5 ng/ml) for 2 days. The experiment was repeated three times. **d** qPCR analysis of mesenchymal marker genes mRNA expression in LX-2 cells overexpressing ATF4 treated with or without increasing concentrations of TGFβ (0, 0.5, 1, and 5 ng/ml) for 2 days ($n = 4$ biological replicates). **e** Western blot showing the expression of fibrotic genes in LX-2-shCtrl and LX-2-shATF4 cells treated with increasing

concentrations of TGFβ (0, 5, and 10 ng/ml) for 2 days. The experiment was repeated four times. **f** qPCR analysis of mRNA expression of fibrotic genes in LX-2-shCtrl and LX-2-shATF4 cells treated with TGFβ for 2 days ($n = 3$ biological replicates). **g** qPCR analysis of mRNA expression of fibrotic genes in LX-2 cells overexpressing ATF4 for 4 days and then treated with increasing concentrations of TGFβ (0, 0.5, and 1 ng/ml) for 2 days ($n = 4$ biological replicates). **h** qPCR analysis of mRNA expression of fibrotic genes in LX-2 cells treated with solvent control (Ctrl), TGFβ (5 ng/ml) for 2 days (TGFβ), or pretreated with ISRIB (1 mM) for 3 days followed by treatment with TGFβ (5 ng/ml) and ISRIB (1 mM) for another 2 days (TGFβ + ISRIB) ($n = 3$ biological replicates). Data are presented as mean \pm s.e.m. and representative of at least three independent experiments. Unpaired, two-tailed Student's t tests were applied for (d) and (f–h). Source data are provided as a Source Data file.

including FN1 and Vimentin, were dramatically increased upon CCl₄ treatment (Fig. 4b), consistent with the upregulation of the EMT program. Fibrotic genes, including *Acta2*, *Col1a1*, and *Col1a2*, were highly induced, indicating HSC activation (Fig. 4b, c; Supplementary Fig. 3f). In contrast, such CCl₄-triggered induction of mesenchymal and fibrotic genes was drastically inhibited in the HSC-*Atf4*-KO animals, suggesting that ATF4 is required for HSC activation in vivo (Fig. 4b, c; Supplementary Fig. 3f). Consistently, the expression of these fibrosis-related genes was also repressed by ATF4 depletion in the primary HSCs (Supplementary Fig. 3g). As the most important markers of fibrosis, type I collagens accumulate during fibrotic progression. *Atf4* deletion markedly lowered the level of hepatic collagen proteins (Fig. 4d, e). Using a hydroxyproline-based assay to quantify the content of

collagen proteins³², we confirmed that HSC-specific *Atf4* deletion significantly reduced the collagen levels (Fig. 4f). Consistently, the pathologic fibrosis progression was effectively alleviated by HSC-specific *Atf4* depletion, as gauged by the serum level of hepatic metabolic enzymes and bilirubin (Fig. 4g). In summary, these results suggest that the expression of ATF4 in HSC is essential for HSC activation and the progression of liver fibrosis.

ATF4 leverages an epigenomic signature of EMT to promote HSC activation

To reveal the underlying mechanisms of how ATF4 regulates the EMT program to promote HSC activation, we interrogated the chromatin binding landscape of ATF4. By conducting ChIP-seq, we found that

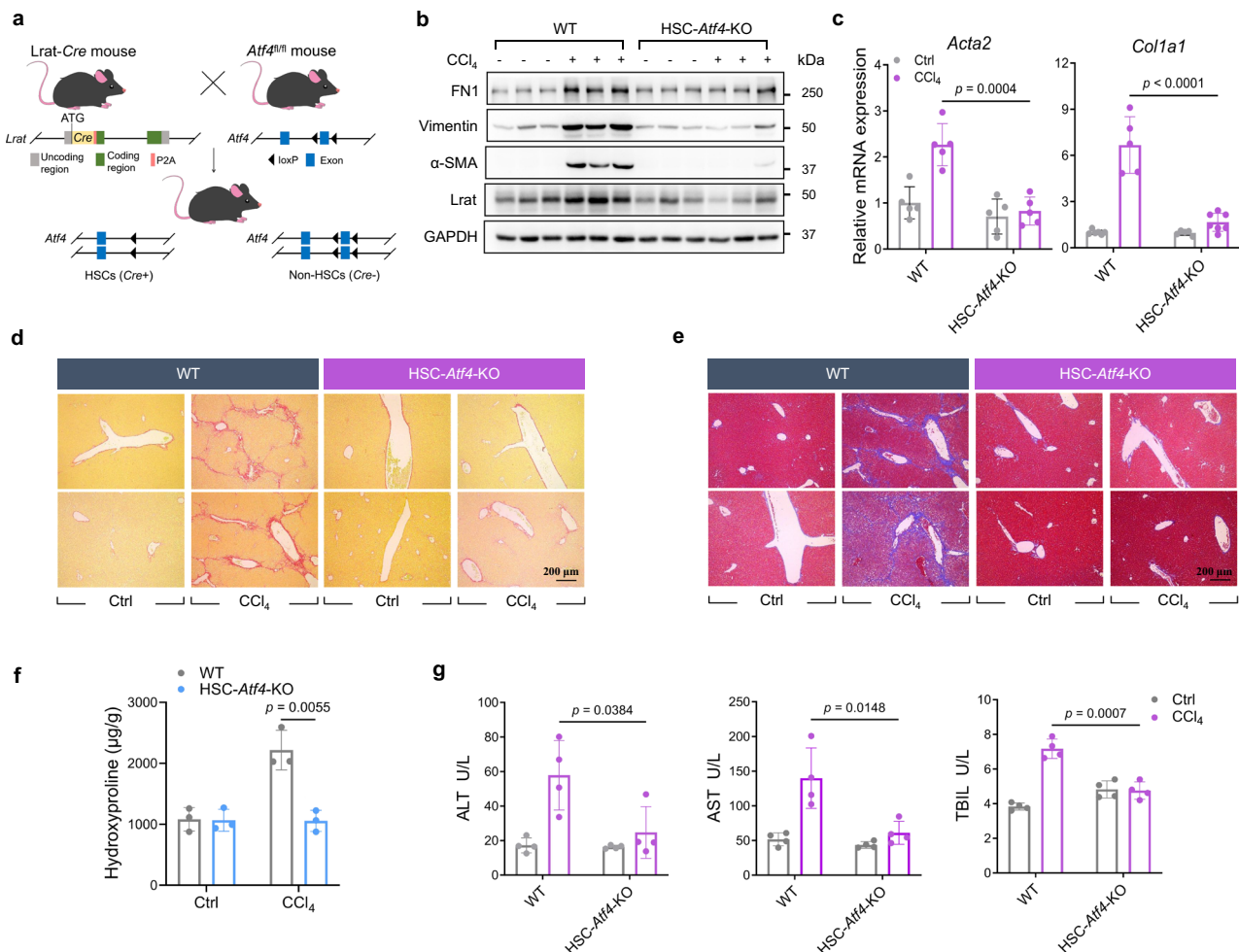


Fig. 4 | HSC-specific depletion of *Atf4* alleviates liver fibrosis in vivo. 8-week-old male Lrat-Cre^{+/+};Atf4^{fl/fl} (WT) and Lrat-Cre^{-/-};Atf4^{fl/fl} (HSC-Atf4-KO) littermates were administrated with CCl₄ (0.5 ml/kg) or solvent control (corn oil) twice weekly for 5 weeks, *n* = 5–7 mice per group. **a** A schematic of the design of Lrat-Cre^{+/+};Atf4^{fl/fl} (HSC-Atf4-KO) mice. **b** Western blots showing the expression of EMT and fibrotic marker genes in the liver tissues of the WT and HSC-Atf4-KO mice. The experiment was repeated three times. **c** qPCR analysis showing the expression of fibrotic marker genes in the liver tissues of (b) (*n* = 5 samples per group). Panels (d, e)

representative images of Sirius red staining and Masson's trichrome staining for liver tissues of (b) (*n* = 6 images derived from 3 mouse livers per group). **f** Hepatic collagen content of the liver tissues of (d) was determined by hydroxyproline quantification (*n* = 3 samples per group). **g**, Serum levels of ALT, AST, and TBIL from the experimental animals of (b) were measured (*n* = 4 samples per group). Data are presented as mean ± s.e.m. Unpaired, two-tailed Student's *t* tests were applied for (c, f, g). Source data are provided as a Source Data file.

ATF4 binds to over 2800 genomic loci in TGFβ-treated LX-2 cells (Fig. 5a). Annotation of these ATF4-bound peaks revealed a striking enrichment of genes involved in the EMT signaling pathway (Fig. 5b). In contrast, in the DMSO- or Tg-treated LX-2 cells, the most significant ATF4-bound gene sets were the ones that regulate protein translation (mTORC1 signaling) and unfolded protein response (Fig. 5a, b; Supplementary Fig. 4a, b). Considering the context-specific roles of ATF4 in regulating gene expression (Fig. 1), these ChIP-seq results support that ATF4 achieves the specificity by binding to distinct genomic regions in response to different signals. Despite the binding selectivity, it appeared that ATF4 bound to its canonical DNA-binding motif no matter whether the LX-2 cells were treated with TGFβ or Tg (Fig. 5c)³³. These results unravel a model that the upstream triggering signals—induction of fibrosis or ER stress—can selectively harness ATF4 to specific chromatin regions to regulate gene transcription.

To test this hypothesis further, we profiled the epigenomic landscape in LX-2 cells under different treatments by conducting ChIP-seq of a well-established active histone marker, the acetylated lysine 27 of Histone 3 (H3K27ac)^{34,35}. Overall, the number of H3K27ac-marked peaks was comparable in LX-2 cells treated either with TGFβ or Tg

(Fig. 5d; Supplementary Fig. 4c). In TGFβ-treated LX-2 cells, most of the ATF4 peaks overlapped with the H3K27ac-marked sites (Fig. 5d, e). Based on signal intensity and coverage, subsets of H3K27ac marked chromatin regions can be designated as super-enhancers (SE) or typical enhancers (TE) (Supplementary Fig. 4d)^{36,37}. While both SE and TE can be important for transcription activation, SE-governed genes more often code for key factors in cell fate determination^{19,37}. We found that over 6% of the ATF4-bound sites were located in SE (ATF4-SE) while about 30% located in TE (ATF4-TE) under TGFβ treatment (Fig. 5f, left panel). Interestingly, ATF4-SE sites exhibited a stronger enrichment for EMT genes than the ATF4-TE sites (Fig. 5f, right panel), suggesting ATF4 preferentially regulates EMT genes via SEs. In contrast, for regulating Tg-induced UPR genes, ATF4 seemed not to preferentially act via SEs (Fig. 5g), despite that its binding peaks showed similar overlapping ratios with SEs or TEs (ATF4-SE 4% and ATF4-TE 16%). These results suggest that ATF4 may utilize the change of epigenomic landscape upon EMT induction to activate gene expression for HSC activation.

We next sought to pinpoint candidate genes that ATF4 bound and directly regulated during EMT induction, and decipher the functional link between epigenetic alteration and ATF4-driven transcription.

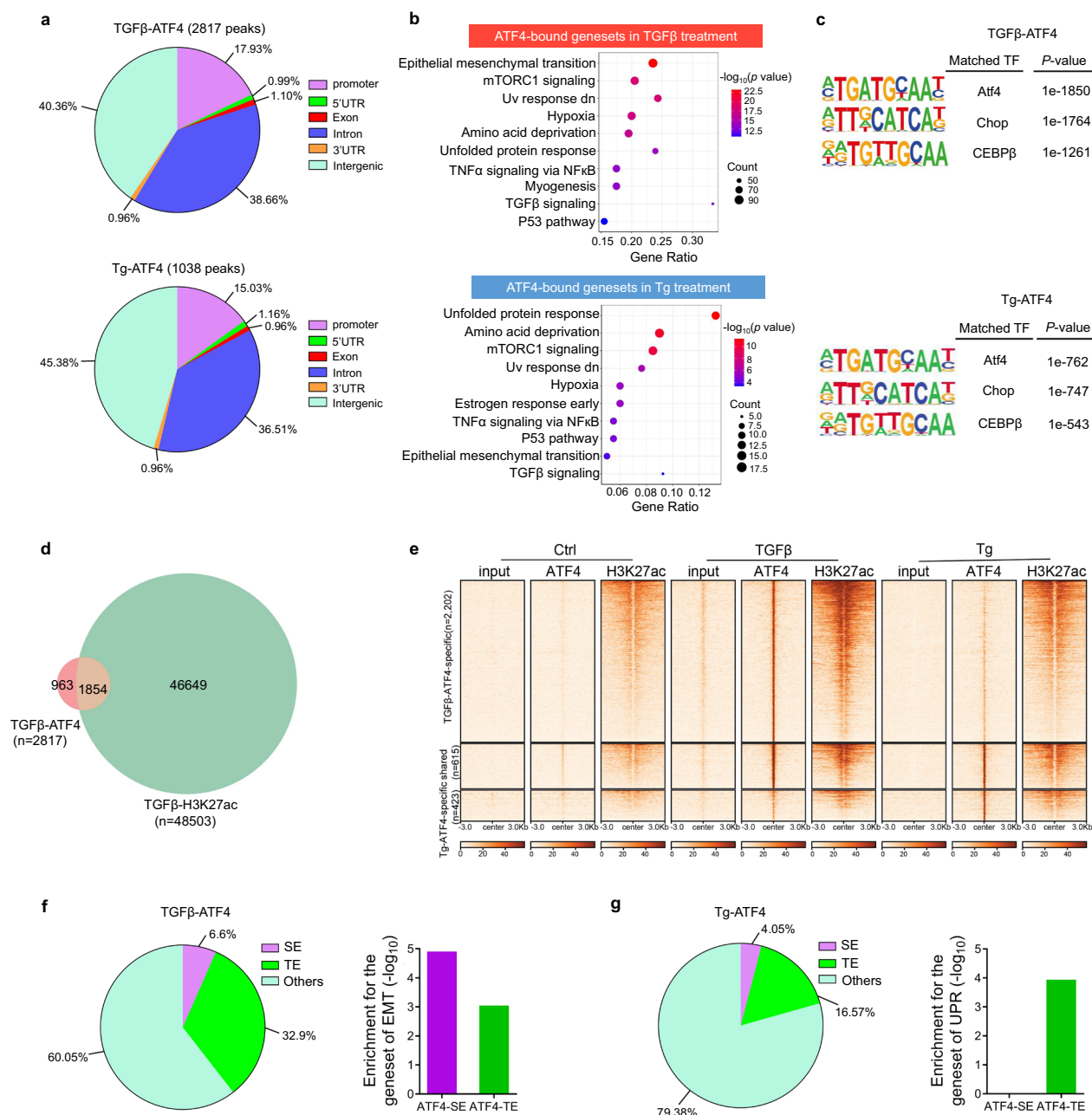


Fig. 5 | The landscape of ATF4 and H3K27ac chromatin binding during HSC activation and ER stress. a The genome-wide distribution of ATF4 binding peaks under TGFβ (TGFβ-ATF4) or Tg (Tg-ATF4) treatment. **b** GO enrichment analysis for genes that are closest to ATF4 binding sites under TGFβ or Tg treatment, respectively. Top enriched pathways were shown. Hypergeometric test was used to identify significant enrichment pathways ($P < 0.01$). **c** DNA-binding motifs of ATF4 under TGFβ or Tg treatment were identified by HOMER. The Top three enriched motifs were shown. **d** Venn diagram summarizing the number of peaks identified by ATF4 and H3K27ac ChIP-seq under TGFβ treatment. **e** The heatmap of normalized ChIP-seq signal of ATF4 and H3K27ac and input in three groups: TGFβ-specific ATF4 binding sites, TGFβ/Tg shared ATF4 binding sites, or Tg-specific ATF4 binding sites

(from top to bottom). **f** Left panel: the distribution of ATF4 binding peaks overlapped with super-enhancers (SE), typical enhancers (TE), or other types of H3K27ac-marked elements (others) under TGFβ treatment. Right panel: the statistical significance of enrichment of the EMT pathway by using genes driven by SE or TE with ATF4 binding (ATF4-SE or ATF4-TE). **g** Left panel: the distribution of ATF4 binding peaks overlapped with super-enhancers (SE), typical enhancers (TE), or other types of H3K27ac-marked elements (others) under Tg treatment. Right panel: the statistical significance of enrichment of the UPR pathway by using genes driven by TE with ATF4 binding (ATF4-TE); the UPR pathway was not enriched by genes driven by SE with ATF4 binding (ATF4-SE).

Many mesenchymal and HSC activation genes were bound by ATF4, including *COL1A1*, *LOXL2*, and *CDH2* (Fig. 6a; Supplementary Fig. 4e). The ATF4 binding regions near *COL1A1* and *LOXL2* can be defined as SEs according to the H3K27ac signals, and the one associated with *CDH2* was defined as TE (Fig. 6a; Supplementary Fig. 4e). ChIP-qPCR confirmed that TGFβ treatment induced the binding of ATF4 to these regions while blockage of the enhancer program by JQ1, an inhibitor of

enhancer activity via targeting BRD4³⁸, repressed the interaction between ATF4 and its binding regions (Fig. 6b). Consistently, interfering histone acetylation by C646, a chemical inhibitor of H3K27ac transferase p300, could also repress the binding of ATF4 to *COL1A1* and *LOXL2* (Supplementary Fig. 4f), further confirming that the TGFβ-initiated epigenetic alteration is required for the re-positioning of ATF4 on the genome.

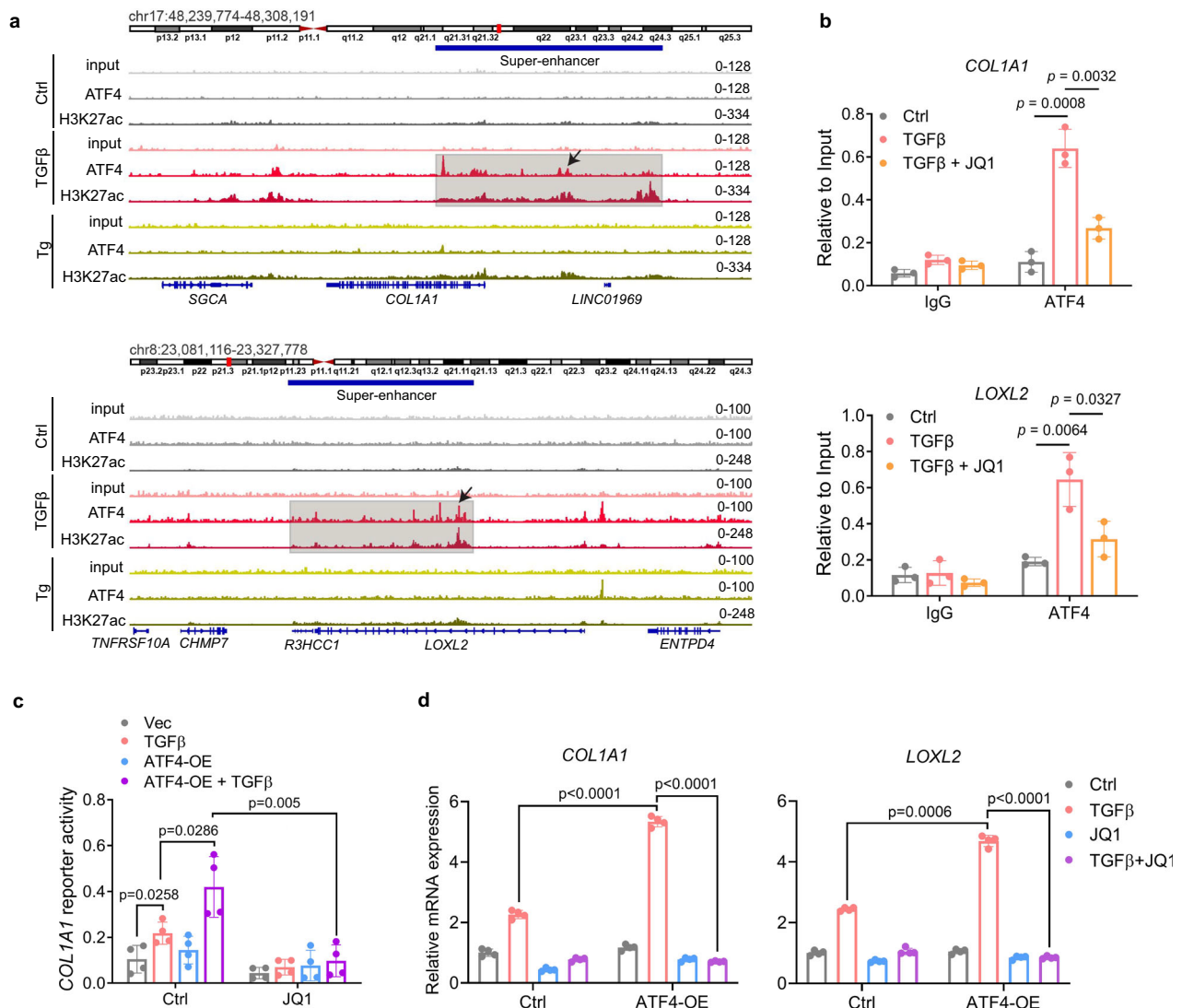


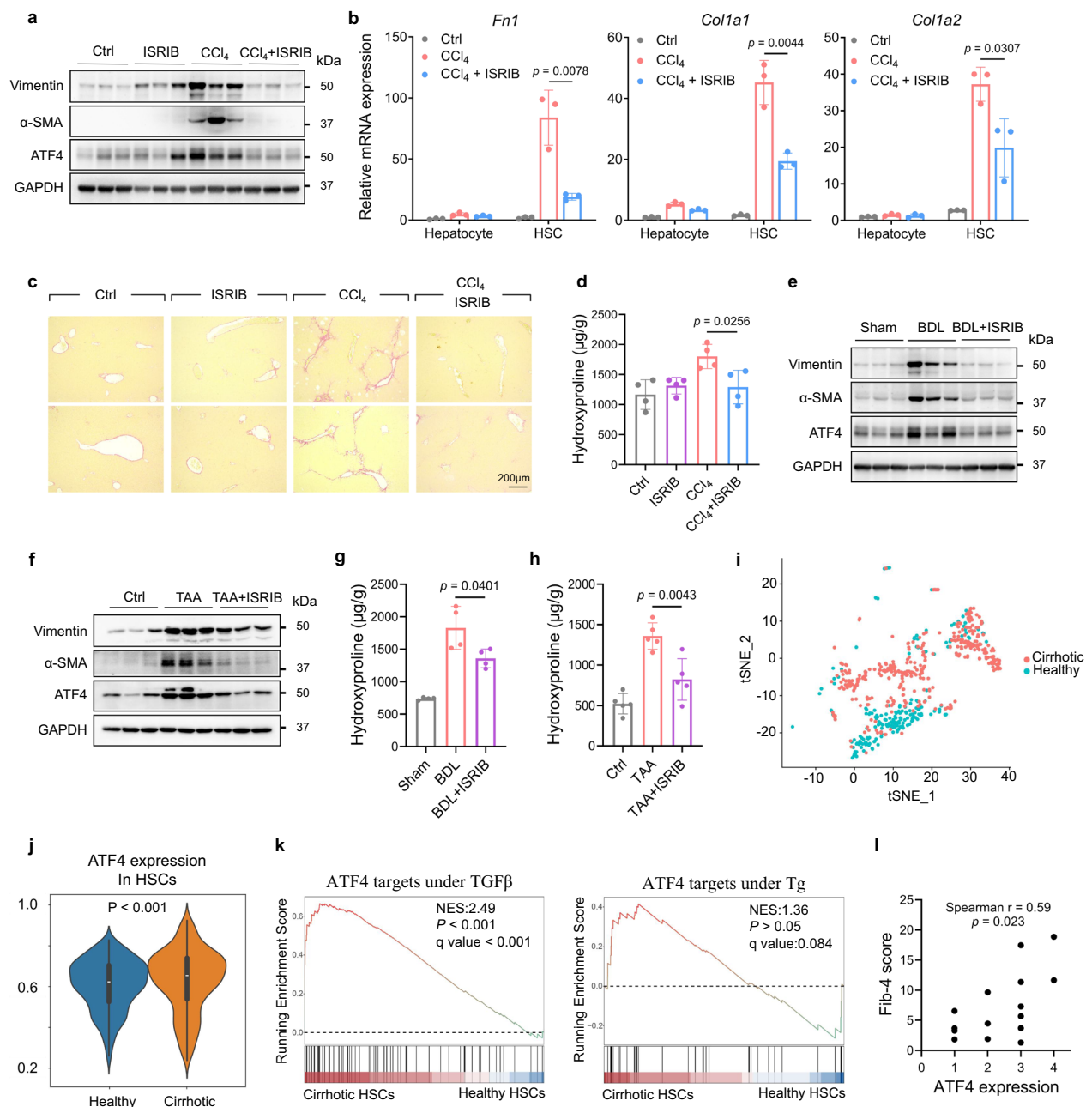
Fig. 6 | ATF4 promotes the transcription of fibrotic genes via enhancer-dependent mechanisms. **a** The snapshots of normalized ATF4 and H3K27ac and input ChIP-seq tracks at *COL1A1* and *LOXL2* loci across different conditions: Ctrl, TGF β , and Tg treatment. The super-enhancers with ATF4 binding sites were highlighted in gray rectangles. The black arrows indicate the binding loci of ATF4, which were adopted for the ChIP-qPCR test. **b** ChIP-qPCR analysis showing the recruitment of ATF4 in the corresponding regions of *COL1A1* and *LOXL2* in the presence of solvent control, TGF β , or combined TGF β and JQ1 ($n = 3$ biological replicates). **c** A luciferase reporter containing a genomic region upstream of the *COL1A1* gene (–9108 to –8708) was constructed to measure the transcriptional activity of the ATF4- and H3K27ac- co-bound regions. The *COL1A1* reporter, along with a Renilla

luciferase reporter, was transfected into LX-2 cells transfected with a control vector (Vec) or an ATF4-overexpression construct (ATF4-OE). The transfected cells were treated with solvent control, TGF β (1 ng/ml) for 2 days, JQ1 (250 nM) for 12 h, or a combination of TGF β (1 ng/ml) for 2 days and JQ1 (250 nM) for 12 h before they were analyzed by the Dual-Luciferase assay ($n = 4$ biological replicates). **d** qPCR analysis showing the expression of *COL1A1* and *LOXL2* in control or LX-2 cells over-expressing ATF4 treated with solvent control, TGF β , JQ1, or a combination of TGF β and JQ1 ($n = 4$ biological replicates). Data are presented as mean \pm s.e.m and representative of at least three independent experiments. Unpaired, two-tailed Student's t tests were applied for (b–d). Source data are provided as a Source Data file.

To validate the functional consequence of ATF4 binding, we established a luciferase-based reporter in which the ATF4-binding site on *COL1A1* was inserted into the regulatory region upstream of the reporter gene. This reporter could respond to TGF β , and overexpression of ATF4 further promoted the transcription of the reporter gene (Fig. 6c). This indicated that ATF4 binding promotes the transcription of *COL1A1* in the presence of TGF β . Consistent with the role of JQ1 in regulating the binding of ATF4 to the *COL1A1* gene, the transcriptional activity of the *COL1A1*-reporter was also abolished by JQ1 (Fig. 6c). Consequently, JQ1 treatment effectively repressed the expression of TGF β -induced, ATF4-dependent genes (Fig. 6d). In a nutshell, we established that ATF4 promotes EMT gene expression in an enhancer-dependent manner.

Pharmacological inhibition of the eIF2 α -ATF4 pathway alleviates liver fibrosis

Our findings on the crucial role of ATF4 in fibrosis have provided an opportunity to treat liver fibrosis by targeting this transcription factor. Indeed, this is pharmacologically feasible since it is known that ISRIB can be used to block ATF4 translation in vivo³⁹. We thus used ISRIB to treat mice with CCl₄-induced liver fibrosis. While ISRIB treatment did not affect the expression of mesenchymal genes in the control cohorts, it resulted in a marked decrease in the CCl₄-induced expression of Vimentin (Fig. 7a). Accordingly, ISRIB treatment also reduced the expression of α -SMA and type I collagens in the liver tissue upon CCl₄ treatment (Fig. 7a; Supplementary Fig. 5a). To examine if the change of fibrotic gene expression occurred in HSCs, we isolated HSCs and hepatocytes from the post-treatment animals and examined their gene



expression. We found that the induced expression of ATF4 in HSCs was repressed by ISRIB, in the meantime the expression of fibrotic genes was also downregulated by ISRIB in HSCs (Fig. 7b; Supplementary Fig. 5b). In comparison, the expression of fibrotic genes in hepatocytes was much lower compared to HSCs, suggesting that the anti-fibrotic effects of ISRIB was mainly through targeting HSCs (Fig. 7b). Consistent with the change in gene expression, accumulation of the collagen proteins was markedly reduced upon ISRIB treatment (Fig. 7c, d; Supplementary Fig. 5c). To test if ISRIB repressed fibrosis by directly alleviating CCl₄-induced hepatocyte death, we examined the expression of a set of cell death markers and found that ISRIB did not alter necrosis or apoptosis caused by acute CCl₄ treatment (Supplementary Fig. 5d). In the TUNEL assay, we found that not only the percentage of hepatocytes with DNA fragmentation was not altered by ISRIB, but the area of necrotic hepatocytes (indicated by light-stained cells with swelling morphology and nuclear shrinkage) was also not changed upon ISRIB treatment (Supplementary Fig. 5e). In addition, CCl₄ treatment did not induce pyroptosis (Supplementary Fig. 5f).

Moreover, ISRIB did not alter the eIF2α pathway in other tissues, including adipose tissues, muscle, and skin (Supplementary Fig. 5g). Together, these data indicate that ISRIB represses CCl₄-triggered liver fibrosis by targeting HSC activation.

In addition to the CCl₄-induced fibrosis, we tested the effects of ISRIB in two additional fibrosis models, one triggered by surgery of bile duct ligation (BDL) and the other induced by thioacetamide (TAA). Consistent with the findings in the CCl₄ model, ISRIB treatment effectively reduced the expression of Vimentin, α-SMA, and type I collagens induced by BDL or TAA, respectively (Fig. 7e, f; Supplementary Fig. 6a, b). Consequently, the BDL- or TAA-induced collagen production and aggregation in the liver were markedly reduced by ISRIB treatment (Fig. 7g, h; Supplementary Fig. 6c–f). Together, these results demonstrate the role of ISRIB in repressing HSC activation during liver fibrogenesis and strongly highlight the potential of ATF4-targeted therapy in treating liver fibrosis.

Lastly, we investigated the clinical relevance of HSC-ATF4 in patients with cirrhosis. To do so, we interrogated a recently published

Fig. 7 | Pharmacological inhibition of eIF2 α -ATF4 alleviates liver fibrosis. **a** 8-week-old male C57BL/6 mice were administered with CCl₄ (0.5 ml/kg) or solvent control (corn oil) and simultaneously with or without ISRIB (5 mg/kg) twice weekly for 5 weeks. $n = 5$ –7 mice per group. Western blots showing the expression of EMT and fibrotic marker genes in the liver tissues of mice with different treatments. The experiment was repeated three times. **b** qPCR analysis showing the expression of fibrotic genes in hepatocytes and HSCs isolated from the liver tissues from **(a)** ($n = 3$ biological replicates). **c** The representative images of Sirius red staining for liver tissues of **(a)** ($n = 6$ images derived from 3 mouse livers per group). **d** The hepatic collagen content of the liver tissues of **(a)** was determined by hydroxyproline quantification ($n = 4$ biological replicates). **e** 8-week-old male C57BL/6 mice underwent a sham (Sham) operation or surgery of common bile duct ligation (BDL), followed by biweekly administration of ISRIB (5 mg/kg) or solvent control for 4 weeks ($n = 5$ mice per group). Western blots showing the expression of EMT and fibrotic marker genes in the liver tissues of mice with different treatments. The experiment was repeated three times. **f** 8-week-old male C57BL/6 mice were administered with solvent control, TAA (150 mg/kg), or a combination of TAA and ISRIB (5 mg/kg) twice weekly for 5 weeks ($n = 5$ mice per group). Western blots showing the expression of EMT and fibrotic marker genes in the liver tissues of mice with different treatments. The experiment was repeated three times. **g** The hepatic collagen content of the liver tissues of **e** was determined by hydroxyproline

quantification ($n = 4$ samples per group). **h** The hepatic collagen content of the liver tissues of **(f)** was determined by hydroxyproline quantification ($n = 5$ samples per group). **i** t-SNE representation of scRNA-seq analysis of HSCs from human liver of healthy donors ($n = 5$) and cirrhotic patients ($n = 5$). Cells from healthy or cirrhotic samples are highlighted in cyan or red, respectively. (adapted from GSE136103). **j** Violin plot showing the mRNA expression of ATF4 in HSCs of **(i)**. **k** GSEA was performed with two genesets of ATF4 targets in a data set where genes were ordered by the fold-change of their expression comparing the HSCs of the cirrhotic patients and the healthy donors of **(i)**. The geneset “ATF4 targets under TGF β ” (left) refers to genes regulated by ATF4 under TGF β treatment in the LX-2 cells originating from the above bulk RNA-seq; The geneset “ATF4 targets under Tg” (right) refers to genes regulated by ATF4 under Tg treatment in the LX-2 cells also originating from the above bulk RNA-seq. The statistical significance (nominal P value) of the normalized enrichment score (NES) was generated by employing an empirical phenotype-based permutation test. **l** Spearman correlation of the Fib-4 scores and the expression of ATF4 in HSCs in the liver tissue from 15 cirrhotic patients. Determined by the intensity of IHC staining, the ATF4 expression in HSCs in these tissues was put into four categories: negative (1), low (2), medium (3), and high (4). Data are presented as mean \pm s.e.m. Unpaired, two-tailed Student's t tests were applied for **(b, d, g, h, j)**. Kolmogorov–Smirnov tests were applied for **(k)**. Spearman's correlation was applied for **(l)**. Source data are provided as a Source Data file.

dataset⁴⁰ in which the non-parenchymal cells (NPCs) of human livers from both healthy donors and patients with cirrhosis were analyzed by scRNA-seq (Fig. 7i; Supplementary Fig. 7a). We found that, compared to the healthy controls, the RNA expression of ATF4 was increased in HSCs from the cirrhotic patients (Fig. 7j). To explore the change of ATF4 on the protein level using the scRNA-seq data, we examined the expression of ATF4-target genes, which can faithfully represent the transcriptional activity of ATF4. By conducting GSEA using the ATF4-regulated genesets derived from the LX-2 cells (Fig. 1d), we found that the ATF4-regulated genes under TGF β treatment (ATF4-TGF β) were significantly upregulated in the HSCs of cirrhotic patients compared to healthy donors (Fig. 7k, left panel). In contrast, the canonical ATF4-regulated genes triggered by ER stress (ATF4-Tg) were not enriched in the context of cirrhosis (Fig. 7k, right panel). These results not only showed an increased activity of ATF4 in the HSCs, but also highlighted the context-dependent role of ATF4 in liver fibrosis. In addition, we examined the relation of ATF4 in fibrosis by investigating the evolutionary relationship between quiescent and active HSCs (qHSCs and aHSCs) using pseudotime trajectory analysis (Supplementary Fig. 7b). We found that the ATF4-TGF β genes were gradually induced during the pseudo-activation of HSC (from qHSC to aHSC, Supplementary Fig. 7c), suggesting that the transcriptional activity of ATF4 increased during HSC activation in patients. To further validate the link between HSC-ATF4 and cirrhosis, we conducted IHC staining for ATF4 in a set of 15 fibrotic liver tissues from patients. We found that the expression of ATF4 in HSCs was significantly correlated with the Fib-4 scores of the patients, which can represent the severity of liver fibrosis (Fig. 7l; Supplementary Fig. 7d, e). These results clearly demonstrate that the expression of ATF4 in HSCs is correlated with the progression of liver fibrosis.

Together, we found that ATF4 is an important pro-fibrotic factor in HSCs, and pharmacological inhibition of ATF4 translation effectively represses liver fibrosis.

Discussion

Activation of HSCs is the major biological event during the onset of liver fibrosis⁸. Compared to the late stages of liver diseases, including cirrhosis and HCC, liver fibrosis is considered controllable and reversible if the essential cellular pathways that drive HSC activation can be effectively targeted². In this study, we identified ATF4 as a key factor required for HSC activation. While largely known as a master regulator in ER stress response, we surprisingly found that ATF4 promotes the activation and transdifferentiation of HSCs via ER stress-independent regulation of the

EMT program a key pathway in cell state determination^{21,41}. It is worth noting that a recent paper also reported the possible involvement of ATF4 in HSC activation and liver fibrosis⁴². However, this article apparently misinterpreted its observations as it applied an AAV8-mediated approach to modify ATF4 expression in the liver, which mainly blocked ATF4 expression in hepatocytes but unfortunately cannot target HSCs^{43–46}. In contrast, in our study we applied an HSC-specific knockout animal-based approach to unambiguously demonstrate that the expression of ATF4 in HSCs is critical for HSC activation. Complimented by the findings that pharmacological inhibition of ATF4 production can effectively alleviate liver fibrosis, our study highlighted a new opportunity for the invention of liver fibrosis in clinic.

Our study revealed a stress-independent function of the eIF2 α -ATF4 stress response pathway in disease progression. Liver fibrosis is a pathological, wound-healing process following chronic or acute liver injuries; therefore, activation of HSC is intuitively considered a cell biological event that inevitably encounters a variety of stressors⁹. For instance, the increase and accumulation of reactive oxygen species (ROS) is a well-established hallmark of liver fibrosis⁴⁷. The pro-fibrotic function of ROS is directly linked to the oxidative stress of HSC since depletion of certain antioxidant proteins (e.g., cytoglobin) makes the animals more susceptible to fibrosis⁴⁸. Similarly, ER stress is frequently observed in liver diseases, including chronic hepatitis and HCC, as gauged by the activation of the UPR pathways in both the hepatocytes and HSCs during liver disease progression^{49,50}. Almost all the previous studies attributed the function of UPR in liver fibrosis to its role in regulating ER homeostasis. A recent report claimed that ATF4 may be involved in HSC activation via regulation of mitochondrial UPR⁴². However, its conclusion remains questionable since the mitochondrial UPR, while very minor, might mainly occur in hepatocytes but not HSCs according to their experimental design. Our findings, for the first time, demonstrated that the UPR factors could drive the progression of liver fibrosis beyond their canonical functions in sensing unfolded proteins and resetting ER milieu. Specifically, we found that ATF4, a master stress response factor, can directly promote the induction of EMT therefore contributing to HSC activation. Our findings implicated that the role of stress response pathways in disease progression might need further evaluation and investigation, since the pathological context may profoundly influence the actual function of these stress pathways.

It is well established that stress response pathways are usually bi-functional. For instance, the UPR pathway could either facilitate an “anti-stress” adaption, allowing cell survival, or it could trigger cell death pathways to wipe out irreversible stressed cells⁵¹. Our study brings the

functional complexity to another level—stress response factors can determine cell fate by regulating EMT, an important cell-state transition program. Despite the many differences between the canonical EMT program and the process of HSC activation, these two cellular events share a very striking common feature—inducing ECM production^{11,15}. According to the findings in this report, we identified another intriguing similarity between EMT and HSC activation—induction of the ATF4-driven signaling, since we have previously reported the PERK-ATF4 branch of the UPR is activated upon cancer cells undergoing an EMT¹⁷. Following its activation, the PERK branch of the UPR can promote drug resistance and metastasis of cancer cells, in addition to its role in surviving cancer cells, particularly the EMT-transformed ones, under ER-stressed conditions¹⁷. Our findings revealed a more fundamental function of the UPR factors by dictating the EMT program.

Our findings shed light on a mode of action of ATF4 in gene transcription. As a canonical UPR factor, it was well established that ATF4 can directly bind to a conserved motif to drive gene transcription during ER stress. Several classical UPR genes, including *GADD34*, *CHOP*, and *ATF3*, are regulated transcriptionally via the ATF4-motif in the promoter regions of these genes^{33,52,53}. Surprisingly, we found while the ATF4-bound DNA motif remains almost the same, the ATF4-driven transcriptome changed dramatically during HSC activation when compared to ER stress. By further analyzing the histone modifications of the new genes targeted by ATF4, we found that ATF4 tends to bind to the enhancer regions during HSC activation. Therefore, we proposed a model that HSC activation, or induction of the EMT program, can reset the landscape of chromosome accessibility, such that ATF4 can be shifted toward the essential genes of HSC activation (e.g., *Col1A1* and *LOXL2*), therefore promoting their transcription. This model is consistent with the previous finding that SMAD2/3, the immediate target of TGF β signaling, could reset the landscape of histone modification to allow for gene transcription regulation by TGF β ⁵⁴. Interestingly, we did not find that the transcription of *SMAD2/3* was regulated by ATF4, which is different than a previous report on the role of ATF4 in regulating the TGF β signaling in breast cancer⁵⁵. It suggests that the interplay between ATF4 and TGF β -SMAD2/3, if any, bears significant differences in HSC compared to cancer cells. In addition, ATF4 may rely on certain epigenomic modifiers to cope with its regulation of the essential HSC activation genes. In fact, it has been reported that ATF4 could work with some histone-modifying enzymes, including KDM4C and Jmjd3, in regulating transcription^{56,57}. Another recent report suggested that ATF4 can cooperate with Myc to modulate the transcription of translational machinery genes in response to the increased bioenergetic demands in cancer⁵⁸. Therefore, it is possible that ATF4 may work with other EMT-TFs to facilitate HSC activation, albeit we did not observe enrichment for any EMT-TFs in the ATF4-ChIP. It will be of particular interest to further investigate the link between ATF4 and classical EMT-TFs, such as Zeb1 and Snail.

Fibrosis remains a reversible, potentially curable stage during liver disease progression. Our findings highlight a strategy and approach to suppress liver fibrosis via inhibiting the eIF2 α -ATF4 signaling pathway. By use of both genetic and chemical interventions, our results not only revealed that ATF4 is an important target of liver fibrosis therapy but also validated that p-eIF2 α , the upstream factor of ATF4, could be a viable target since chemical inhibition of p-eIF2 α can effectively repress the development of liver fibrosis in mice. The chemical inhibitor of p-eIF2 α , ISRIB, was developed by Peter Walters's group a few years back, and it has been applied in a series of tests of neuronal syndromes^{29,59}. It was shown that ISRIB has neuroprotective effects. It improves memory in aged and traumatic brain injury mice^{60–63}, prevents neurodegeneration in prion-diseased mice⁶⁴, reduces neuropathic pain induced by diabetes⁶⁵, and rescues the impaired sociability and anxiety-like behavior in adult *caecalC*-deficient mice⁶⁶. Interestingly, another group recently found that ISRIB appeared effective in attenuating pulmonary fibrosis by promoting the post-injury regeneration of pulmonary epithelium⁶⁷.

Although the underlying mechanism varies, the encouraging results in lung fibrosis implicate the great potential of ISRIB in treating fibrotic diseases of other origins. Most importantly, the safety of targeting the eIF2 α -ATF4 pathway has not only been reported in many animal studies^{60–66}, but it was also validated by a recent phase I trial on Amyotrophic Lateral Sclerosis⁶⁸. While several key drivers of liver fibrosis have been documented (such as TGF β -driven signaling), the substantial toxicity of blocking these pathways has been hindering the development of fibrosis-targeted therapy. Considering the advantages of both safety and efficacy, targeting the eIF2 α -ATF4 pathway appears a promising, viable strategy in the intervention of liver fibrosis.

Methods

All research conducted for this manuscript complies with ethical regulations. All mice experiments were approved by the Institutional Animal Care and Use Committee of Zhejiang University and comply with all regulations for the ethical conduct of research.

Cell culture and reagents

HMLE and HMLER cells expressing the coding sequence of Twist-ER or Snail were generated from Dr. Robert A. Weinberg's laboratory and maintained in a 1:1 mixture of DMEM + 5% FBS, insulin (10 μ g/ml), EGF (10 ng/ml), hydrocortisone (0.5 μ g/ml), and Mammary Epithelial Cell Growth Medium (MEGM). The Twist-ER transgene was activated upon 4-hydroxytamoxifen (4-OHT) treatment. The Snail transgene was induced by doxycycline (DOX). The LX-2 cell line was purchased from Biobank, Xiangya School of Medicine, Central South University, and was cultured in DMEM + 10% FBS. The AML12 cell line was purchased from National Collection of Authenticated Cell Cultures, and was cultured with special medium (National Collection of Authenticated Cell Cultures, SCSP-654), including 89% DMEM/F-12 culture medium (1:1) (Gibco, 11330032), 10% Fetal bovine serum (FBS) (Gibco), 1% ITS liquid culture supplement (Sigma, I3146), and adding dexamethasone to the final concentration of 40 ng/ml. Phosphorated eIF2 α inhibitor ISRIB (B3699) was purchased from APExBIO. TGF β (7754-BH-005) was obtained from R&D Systems. CCL₄ (C805329) was purchased from MACKUN. PDGF-BB (220-BB) was purchased from Novus Biologicals. C646 (S7152) and TAA (E0156) were purchased from Selleck.

Quantitative PCR

Following the indicated treatments, mRNA was harvested using an RNeasy Kit (Qiagen) according to the manufacturer's protocol. mRNA was reverse transcribed using cDNA synthesis kits (BIO-RAD), and the primers used for quantitative PCR (qPCR) were outlined in Supplementary Table 1.

Immunoblotting

Following the indicated treatments, whole cells or tissue lysates were harvested using RIPA buffer. The lysates were separated by SDS-PAGE, transferred to polyvinylidene fluoride membrane, and blotted with the following antibodies. ATF4 (11815), ZEB1(70512), E-Cadherin (3195), N-Cadherin (13116), Vimentin (5741), Snail (3879), Slug (9585), Claudin-1 (13255), α -Smooth muscle actin (19245), CHOP (2895), cleaved Caspase-1 (4199), cleaved PARP (5625) and p-RIP3 (93654) antibodies were purchased from Cell Signaling Technology. FN1 (F3648) antibody was purchased from Sigma-Aldrich. GAPDH (ARG10112) and Actin (ARG66382) antibodies were purchased from Arigo Biolaboratories. Tubulin (BX00009-C3) antibody was purchased from Biolynx. Lat (sc-101391) and another ATF4 (sc-390063) antibodies were purchased from Santa Cruz Biotechnology. GSDMD (ab209845) antibody was purchased from Abcam.

Transwell assay

Following the indicated treatments, cells were digested and seeded into the Transwell chamber (Corning). After migrating for 8 h, cells

were stained with Calcein-AM (BD Bioscience, 354216), and images of stained cells were taken with a camera-installed microscope at 10× objective. ImageJ was used to analyze images quantitatively.

Flow cytometry analysis

Cells were stained with CD24-PE (BD Bioscience, 555428) and CD44-APC (BD Bioscience, 559942) antibodies for 30 min according to the manufacturer's protocol (BD Bioscience). After staining, cells were washed with PBS twice and resuspended with PBS containing 2% FBS. The stained cells were analyzed with a Beckman flow cytometer.

Plasmid construction

PCR-amplified human wild-type *ATF4* was cloned into the pCW57.1/puro (+)-Flag, -HA, -V5 vector. The pGL3-COL1A1-enhancer plasmids were constructed by PCR-amplifying COL1A1-enhancers (-9108–-8708) and separately inserted into a pGL3-enhancer vector. The oligonucleotides targeting human *ATF4* were constructed into an Age I/EcoR I-digested pLKO.1-puro/blast vector and thus yielded shRNAs targeting *ATF4*. The primers for the above plasmids were summarized in Supplementary Table 2.

Isolation of hepatic stellate cells

Primary mouse HSCs were isolated using the method based on retrograde pronase-collagenase perfusion of the liver and subsequent density-gradient centrifugation as previously described⁶⁹. Buffer solutions were made prior to isolation, including EGTA solution, enzyme solution, GBSS/A (Gey's balanced salt solution A) solution, GBSS/B (Gey's balanced salt solution B) solution, and Nycodenz solution. The perfusion pump with the commercial model (Longer pump, BT 100-2J) was set up. Animals were then anesthetized, and the livers were perfused with the EGTA solution, protease solution, and collagenase solution. Upon termination of perfusion, the liver tissue was further digested with the mixed solution of protease, collagenase, and DNA I enzyme solution in a water bath. Neutralize the hepatocyte suspension with GBSS/B after digestion, and sequentially perform procedures such as sieving, centrifugation, resuspension, and a second centrifugation. Next, mix the washed cells with Nycodenz solution to prepare a gradient solution, followed by density gradient centrifugation. After centrifugation, low-density HSCs can be collected from the upper layer, followed by cell counting, plating, and other relevant assays. Protein and mRNA of HSCs were harvested after HSCs were isolated freshly.

Bulk RNA-seq analysis

Total RNA was extracted following the protocol provided by Qiagen RNeasy Kit. Briefly, oligo(dT) beads were used to enrich mRNA. After fragmentation, the cDNA libraries were made using NEBNext Ultra RNA Library Prep Kit for Illumina (New England Biolabs) and were assessed by using a Qubit 2.0 fluorometer to calculate the concentrations and a Bioanalyzer Instrument to determine the size of the inserted fragment. cDNA library samples were then sequenced by using the PE150 sequencing platform in the Novogene company. The bcl2fastq was used for demultiplexing.

The raw reads with illumina universal adapters and low-quality bases were trimmed by Cutadapt. Then, the remaining reads were aligned to the hg38 genome using STAR. Only unique mapped reads were kept for further analysis. Gene counts were calculated by using feature Counts with default parameters. The DESeq2 package was used to identify differentially expressed genes with the cutoff: $|\log_2 \text{fold change}| \geq 1.5$ and $p < 0.05$.

Gene ontology (GO) and gene set enrichment analysis (GSEA) were conducted using the hallmark signature genesets from the Molecular Signature Database (MSigDB, Broad Institute), with an additional geneset "Amino Acid Deprivation" comprising the top 200 genes induced by an aminopeptidase inhibitor, CHR-2797, to mimic the condition of amino acid deprivation⁷⁰.

Chromatin immunoprecipitation (ChIP) assay

We performed chromatin immunoprecipitation (ChIP) assay primarily according to the instructions of the ChIP assay kit (Cell Signaling Technology, 9003) with minor modifications. We adopted about 2×10^7 LX-2 cells for each IP. When reagent treatment was finished, cells were first fixed with formaldehyde for 10 min and terminated with 10× glycine immediately. Then, the cell membrane was lysated, and the cell nuclear membrane was permeabilized to yield prepared nuclei. Micrococcal nuclease was used to digest chromatin, and the quantity of micrococcal nuclease should be strictly tested according to the size of DNA bands. After chromatin in nuclei was digested, we used ultrasound to break the nuclei membrane. The ultrasonic parameters should be adjusted carefully according to the degree of nuclear fragmentation. The following steps, including chromatin immunoprecipitation, elution of chromatin from antibody/protein G magnetic beads and reversal of cross-links, and DNA purification, were performed according to the standard protocol. The adopted antibodies included anti-ATF4 (Cell Signaling Technology, 11815) and anti-histone H3 (acetyl K27) (Abcam, 4729). Finally, the purified and immunoprecipitated DNA was analyzed by qPCR or next-generation sequencing.

ChIP-seq analysis

The purified and immunoprecipitated DNA fragments (100–500 base pairs) were prepared for Solexa (Illumina) sequencing according to the manufacturer's instructions. ChIP-seq library was sent to the BGI company and sequenced by using an MGISEQ-2000 sequencing machine. SAM tools were used to remove low-quality mapping reads ("q 10"), PCR duplicates, and mitochondrial reads. After removing adaptors and low-quality bases, the single-end reads were mapped to hg19 reference genome by Bowtie2. HOMER was used for peak calling. For ChIP-seq visualization, each ChIP-seq library was normalized to RPKM, and then the genome-wide track for each library was generated using bamCoverage with built-in deep tools. Two peaks with one bp overlapping were considered as overlays by using Bed tools.

Motif analysis

HOMER was used to find motifs which appeared within ChIP-seq peaks, using default parameters, that is the "-mask" parameter used only with repeat-masked sequences. The background sequences were randomly selected from the genome, matched for GC% content.

Super-enhancer identification

HOMER was used to identify the enrichment regions of H3K27ac. The H3K27ac peak regions overlapping within a window ± 2 kb around TSS were excluded for downstream analysis. Super-enhancers were identified using ROSE (Rank Ordering of SE) which stitches the remaining H3K27ac peaks as enhancers together, if they are within 12.5 kb genomic distance, and ranked the enhancers by their input-subtracted intensity/score of H3K27ac³⁷. Those regions are sorted by the score, normalized by the highest score and the number of estimated enhancer regions, and regions past the point where the slope is greater than 1 are identified as SEs.

Luciferase reporter assay

Inducible ATF4-overexpressed LX-2 cell (LX-2-ATF4-DOX) was used to co-transfected with 500 ng COL1A1-PGL3 plasmid and 40 ng Renilla plasmid for 48 h in one well of a 24-well plate. During the transfection, doxycycline (1 $\mu\text{g}/\text{ml}$) was added for 4 days, TGF β (1 ng/ml) was added for 2 days, and JQ1 was added for 12 h. After the indicated treatment, cells were lysed, and chemo-luminescence intensity was detected according to the manufacturer's instructions of the Dual-Luciferase Reporter Assay System (Promega, E1910).

Animal studies

All the mice were housed in a temperature-controlled room (20–25°C) with 50–65% humidity, with a light/dark cycle of 12/12 h. All mice experiments were approved by the Institutional Animal Care and Use Committee of Zhejiang University. *Lrat-Cre* mice were purchased from GemPharmatech, and cre endonuclease was inserted following the *Lrat* gene starting code. A male *Atf4^{fl/m}* mouse was from Dr. Jinghai Chen's laboratory at Zhejiang University. The conditional HSC-specific *Atf4*-knockout mice were obtained by crossing *Atf4^{fl/m}* mice with *Lrat-Cre* mice.

We used 8- to 12-week-old male mice for experimental procedures. For the CCl₄-induced liver fibrosis model, CCl₄ (MACKUN) (0.7 ml/kg body weight and 1:5 diluted in corn oil) was administered intraperitoneally twice a week for 5 weeks. For the TAA-induced liver fibrosis model, TAA (Selleck) (150 mg/kg body weight) was administered intraperitoneally twice a week for 5 weeks. For ISRIB treatment, mice were intraperitoneally injected with ISRIB (5 mg/kg body weight) twice a week for 5 weeks. ISRIB was first dissolved with DMSO to prepare a 5 mg/ml stock solution and then diluted with a mixture of PBS and PEG400 (1:1), thus resulting in a working ISRIB solution with a concentration of 1.25 mg/ml. Cholestasis-dependent fibrosis was induced by surgical ligation of the common bile duct under pentobarbital sodium anesthesia. The common bile duct is separated bluntly and ligating at both ends, then cut in the middle of the ligature, assisted by a stereomicroscope. Mice that underwent laparotomy but were not ligated simultaneously served as controls (sham).

Hydroxyproline detection

Weigh fresh or frozen liver tissues and add 6 M HCl to obtain a ~100 mg tissue/ml solution. Incubate the liver tissues and the prepared collagen standard at 95 °C for 20 h in a thermal block, then cool to room temperature. Subsequent steps were performed according to the manufacturer's instructions for the Sensitive Tissue Collagen Assay kit (QuickZyme Bioscience). The optical density of each sample and standard was measured at 570 nm.

Collagen staining of liver

Liver specimens were fixed in 4% buffered formalin immediately after necropsy and embedded in paraffin. 4 µm liver sections were stained with picro-sirius red (Servicebio, GC307014) or Masson tri-color dye solution (Servicebio, G1006) according to the manufacturer's instructions. Liver fibrosis was assessed quantitatively by measurement of Sirius-red or Masson-blue positive area on 10 representative fields (10× magnification) per sample using ImageJ software.

Preprocessing 10× scRNA-seq data

Raw sequencing files for gene expression libraries were collected from a previous paper⁴⁰. After aligning the raw reads of each sample to the hg38 reference genome by cellranger-7.0.1, the ambient RNA for each cell was estimated and removed by Cellbender⁷¹. Doublet cells were then identified using Scrublet from the filtered feature barcode matrices generated by Cellbender⁷². Cells were scored as candidate doublets by Scrublet and removed if the doublet score exceeded 0.20. Finally, remaining cells were filtered to have less than 5% of their UMI's mapped to mitochondrial genes and to express greater than 200 genes by Scanpy⁷³.

Dimensionality reduction and clustering analysis

Scanpy pipeline (v1.10.2) was employed for single-cell analysis. Raw counts for each cell were transformed by log-normalized via `scanpy.pp.log1p()` and subsequently used to select 3,000 highly variable genes (`scanpy.pp.highly_variable_genes()`). Single cells were batch corrected and projected into a low-dimensional representation by single cell Variational Inference (scvi; scvitools v1.1.2)⁷⁴. The raw counts of the highly variable genes were used to train the scVI VAE model (parameters: `batch_key = 'Sex'` and `'FACS (CD45+ or CD45-)'` and `"Individuals"` and

`"conditions (healthy or disease)"`, `n_latent = 15`). The 15 latent dimensions were used to determine a KNN graph with running `scanpy.pp.neighbors (n_neighbors = 15)` for UMAP generation (`scanpy.tl.umap()`) and leiden clustering (`scanpy.tl.leiden (resolution=1.5, 1.2 or 1)`). Major cell types and Subclusters were marked and identified using well-known marker genes, quality control metrics and gene lists provided by `'scanpy.tl.rank_genes_groups'`.

RNA velocity and pseudo-time trajectory analysis

Spliced and unspliced transcript counts were calculated by the `run10x` command from `velocyto`⁷⁵. Spliced and unspliced gene counts were normalized and smoothed across 20 nearest neighbors using the `filter_and_normalize` and `moments` functions from the `scVelo`⁷⁶. Then, Global scVelo RNA velocity, transition matrix estimates and streamline visualizations were calculated using the `velocity` and `velocity_embedding_stream` functions from the `scVelo` package with Dynamical Modeling. The Normalized spliced and unspliced transcript counts serve as the input matrix for the pseudotime trajectory inferred by `scanpy.tl.diffmap()` and `scanpy.tl.dpt()` and the visualization of pseudotime UMAP by `scv.pl.scatter()`.

Human liver tissues

The human liver tissues used in this study were obtained from patients with liver diseases who underwent treatment in the First Affiliated Hospital, Zhejiang University School of Medicine. All patients selected for the study gave informed consent, and the study was approved by the Ethical Committee of First Affiliated Hospital, Zhejiang University School of Medicine.

Statistical analysis

The measurement data in this study were statistically analyzed by Excel or GraphPad Prism 8.0 software and presented as Mean ± SEM unless otherwise indicated. Image information was extracted using Image J software. Student's *t* test was used for comparative analysis between two data groups, and ANOVA test was used for comparative analysis between multiple data groups. *P* values < 0.05 with a 95% confidence interval were considered significant.

Reporting summary

Further information on research design is available in the Nature Portfolio Reporting Summary linked to this article.

Data availability

Bulk RNA-seq and ChIP-seq data from this study have been deposited in NCBI with accession number: <https://www.ncbi.nlm.nih.gov/geo/query/acc.cgi?acc=GSE235786>. The human scRNA-seq data used in this study are available in the GEO DataSets under accession code [GSE136103](https://www.ncbi.nlm.nih.gov/geo/query/acc.cgi?acc=GSE136103). All remaining data can be found in the Article, Supplementary, or Source data files. All other data and materials are available from the corresponding author upon request. Source data are provided with this paper.

References

- Hernandez-Gea, V. & Friedman, S. L. Pathogenesis of liver fibrosis. *Annu Rev. Pathol.* **6**, 425–456 (2011).
- Kisseleva, T. & Brenner, D. Molecular and cellular mechanisms of liver fibrosis and its regression. *Nat. Rev. Gastroenterol. Hepatol.* **18**, 151–166 (2021).
- Cotter, T. G. & Rinella, M. Fatty liver disease 2020: The state of the disease. *Gastroenterology* **158**, 1851–1864 (2020).
- Schwabe, R. F., Tabas, I. & Pajvani, U. B. Mechanisms of fibrosis development in nonalcoholic steatohepatitis. *Gastroenterology* **158**, 1913–1928 (2020).
- Parola, M. & Pinzani, M. Liver fibrosis: Pathophysiology, pathogenetic targets and clinical issues. *Mol. Asp. Med.* **65**, 37–55 (2019).

6. Kim, E. & Viatour, P. Hepatocellular carcinoma: Old friends and new tricks. *Exp. Mol. Med.* **52**, 1898–1907 (2020).
7. Zhao, M. et al. Targeting fibrosis, mechanisms and clinical trials. *Signal Transduct. Target Ther.* **7**, 206 (2022).
8. Wang, S. S. et al. Perivascular stellate cells are the main source of myofibroblasts and cancer-associated fibroblasts formed after chronic liver injuries. *Hepatology* **74**, 1578–1594 (2021).
9. Friedman, S. L. Hepatic stellate cells: protean, multifunctional, and enigmatic cells of the liver. *Physiol. Rev.* **88**, 125–172 (2008).
10. Higashi, T., Friedman, S. L. & Hoshida, Y. Hepatic stellate cells as key target in liver fibrosis. *Adv. Drug Deliv. Rev.* **121**, 27–42 (2017).
11. Tsuchida, T. & Friedman, S. L. Mechanisms of hepatic stellate cell activation. *Nat. Rev. Gastroenterol. Hepatol.* **14**, 397–411 (2017).
12. Kalluri, R. & Neilson, E. G. Epithelial-mesenchymal transition and its implications for fibrosis. *J. Clin. Invest.* **112**, 1776–1784 (2003).
13. Duffield, J. S., Luyker, M., Thannickal, V. J. & Wynn, T. A. Host responses in tissue repair and fibrosis. *Annu. Rev. Pathol.* **8**, 241–276 (2013).
14. Chaffer, C. L., San Juan, B. P., Lim, E. & Weinberg, R. A. EMT, cell plasticity and metastasis. *Cancer Metastasis Rev.* **35**, 645–654 (2016).
15. Lamouille, S., Xu, J. & Derynck, R. Molecular mechanisms of epithelial-mesenchymal transition. *Nat. Rev. Mol. Cell Biol.* **15**, 178–196 (2014).
16. Masola, V. et al. In vitro effects of interleukin (IL)-1 beta inhibition on the epithelial-to-mesenchymal transition (EMT) of renal tubular and hepatic stellate cells. *J. Transl. Med.* **17**, 12 (2019).
17. Feng, Y. X. et al. Epithelial-to-mesenchymal transition activates PERK-eIF2 α and sensitizes cells to endoplasmic reticulum stress. *Cancer Discov.* **4**, 702–715 (2014).
18. Schroder, M. & Kaufman, R. J. The mammalian unfolded protein response. *Annu. Rev. Biochem.* **74**, 739–789 (2005).
19. Whyte, W. A. et al. Master transcription factors and mediator establish super-enhancers at key cell identity genes. *Cell* **153**, 307–319 (2013).
20. Lu, S. et al. Transcriptional control of metastasis by integrated stress response signaling. *Front. Oncol.* **11**, 770843 (2021).
21. Wortel, I. M. N., van der Meer, L. T., Kilberg, M. S. & van Leeuwen, F. N. Surviving stress: Modulation of ATF4-mediated stress responses in normal and malignant cells. *Trends Endocrinol. Metab.* **28**, 794–806 (2017).
22. Recouvreur, M. V. et al. Glutamine depletion regulates Slug to promote EMT and metastasis in pancreatic cancer. *J. Exp. Med.* **217**, e20200388 (2020).
23. Suzuki, T., Osumi, N. & Wakamatsu, Y. Stabilization of ATF4 protein is required for the regulation of epithelial-mesenchymal transition of the avian neural crest. *Dev. Biol.* **344**, 658–668 (2010).
24. Verwilst, P. et al. Revealing protein aggregates under thapsigargin-induced ER stress using an ER-targeted thioflavin. *ACS Sens.* **4**, 2858–2863 (2019).
25. Kilberg, M. S., Shan, J. & Su, N. ATF4-dependent transcription mediates signaling of amino acid limitation. *Trends Endocrinol. Metab.* **20**, 436–443 (2009).
26. Dewidar, B., Meyer, C., Dooley, S. & Meindl-Beinker, A. N. TGF- β in hepatic stellate cell activation and liver fibrogenesis-updated 2019. *Cells* **8**, 1419 (2019).
27. Xu, L. et al. Human hepatic stellate cell lines, LX-1 and LX-2: new tools for analysis of hepatic fibrosis. *Gut* **54**, 142–151 (2005).
28. Mani, S. A. et al. The epithelial-mesenchymal transition generates cells with properties of stem cells. *Cell* **133**, 704–715 (2008).
29. Tsai, J. C. et al. Structure of the nucleotide exchange factor eIF2B reveals mechanism of memory-enhancing molecule. *Science* **359**, eaq0939 (2018).
30. Gandhi, C. R. Hepatic stellate cell activation and pro-fibrogenic signals. *J. Hepatol.* **67**, 1104–1105 (2017).
31. Liu, X. et al. Identification of lineage-specific transcription factors that prevent activation of hepatic stellate cells and promote fibrosis resolution. *Gastroenterology* **158**, 1728–1744.e1714 (2020).
32. McHedlidze, T. et al. Interleukin-33-dependent innate lymphoid cells mediate hepatic fibrosis. *Immunity* **39**, 357–371 (2013).
33. Shan, J. et al. The C/ebp-Atf response element (CARE) location reveals two distinct Atf4-dependent, elongation-mediated mechanisms for transcriptional induction of aminoacyl-tRNA synthetase genes in response to amino acid limitation. *Nucleic Acids Res.* **44**, 9719–9732 (2016).
34. Beacon, T. H. et al. The dynamic broad epigenetic (H3K4me3, H3K27ac) domain as a mark of essential genes. *Clin. Epigenetics* **13**, 138 (2021).
35. Pelham-Webb, B. et al. H3K27ac bookmarking promotes rapid post-mitotic activation of the pluripotent stem cell program without impacting 3D chromatin reorganization. *Mol. Cell* **81**, 1732–1748.e1738 (2021).
36. Blobel, G. A., Higgs, D. R., Mitchell, J. A., Notani, D. & Young, R. A. Testing the super-enhancer concept. *Nat. Rev. Genet.* **22**, 749–755 (2021).
37. Hnisz, D. et al. Super-enhancers in the control of cell identity and disease. *Cell* **155**, 934–947 (2013).
38. Loven, J. et al. Selective inhibition of tumor oncogenes by disruption of super-enhancers. *Cell* **153**, 320–334 (2013).
39. Anand, A. A. & Walter, P. Structural insights into ISRIB, a memory-enhancing inhibitor of the integrated stress response. *FEBS J.* **287**, 239–245 (2020).
40. Ramachandran, P. et al. Resolving the fibrotic niche of human liver cirrhosis at single-cell level. *Nature* **575**, 512–518 (2019).
41. Li, X., Pei, D. & Zheng, H. Transitions between epithelial and mesenchymal states during cell fate conversions. *Protein Cell* **5**, 580–591 (2014).
42. Ye, M. P. et al. Mitochondrial stress induces hepatic stellate cell activation in response to the ATF4/TRIB3 pathway stimulation. *J. Gastroenterol.* **58**, 668–681 (2023).
43. Sands, M. S. AAV-mediated liver-directed gene therapy. *Methods Mol. Biol.* **807**, 141–157 (2011).
44. Ho, K. J. et al. Optimized adeno-associated virus 8 produces hepatocyte-specific Cre-mediated recombination without toxicity or affecting liver regeneration. *Am. J. Physiol. Gastrointest. Liver Physiol.* **295**, G412–G419 (2008).
45. Cabanes-Creus, M. et al. Novel human liver-tropic AAV variants define transferable domains that markedly enhance the human tropism of AAV7 and AAV8. *Mol. Ther. Methods Clin. Dev.* **24**, 88–101 (2022).
46. Zhang, Z. et al. ANGPTL8 accelerates liver fibrosis mediated by HFD-induced inflammatory activity via LILRB2/ERK signaling pathways. *J. Adv. Res.* **47**, 41–56 (2023).
47. Ramos-Tovar, E. & Muriel, P. Molecular mechanisms that link oxidative stress, inflammation, and fibrosis in the liver. *Antioxid. (Basel)* **9**, 1279 (2020).
48. Okina, Y. et al. TGF- β 1-driven reduction of cytoglobin leads to oxidative DNA damage in stellate cells during nonalcoholic steatohepatitis. *J. Hepatol.* **73**, 882–895 (2020).
49. Li, X. et al. Endoplasmic reticulum stress is the crossroads of autophagy, inflammation, and apoptosis signaling pathways and participates in liver fibrosis. *Inflamm. Res.* **64**, 1–7 (2015).
50. Xia, S. W. et al. Endoplasmic reticulum stress and protein degradation in chronic liver disease. *Pharm. Res.* **161**, 105218 (2020).
51. Hetz, C., Zhang, K. & Kaufman, R. J. Mechanisms, regulation and functions of the unfolded protein response. *Nat. Rev. Mol. Cell Biol.* **21**, 421–438 (2020).
52. Cherasse, Y. et al. The p300/CBP-associated factor (PCAF) is a cofactor of ATF4 for amino acid-regulated transcription of CHOP. *Nucleic Acids Res.* **35**, 5954–5965 (2007).

53. Oh-Hashi, K., Sugiura, N., Amaya, F., Isobe, K. I. & Hirata, Y. Functional validation of ATF4 and GADD34 in Neuro2a cells by CRISPR/Cas9-mediated genome editing. *Mol. Cell Biochem.* **440**, 65–75 (2018).
54. Aseem, S. O. et al. Epigenomic evaluation of cholangiocyte transforming growth factor- β signaling identifies a selective role for histone 3 lysine 9 acetylation in biliary fibrosis. *Gastroenterology* **160**, 889–905 e810 (2021).
55. Gonzalez-Gonzalez, A. et al. Activating transcription factor 4 modulates TGF β -induced aggressiveness in triple-negative breast cancer via SMAD2/3/4 and mTORC2 signaling. *Clin. Cancer Res.* **24**, 5697–5709 (2018).
56. Zhao, E. et al. KDM4C and ATF4 cooperate in transcriptional control of amino acid metabolism. *Cell Rep.* **14**, 506–519 (2016).
57. Shan, J., Fu, L., Balasubramanian, M. N., Anthony, T. & Kilberg, M. S. ATF4-dependent regulation of the JMJD3 gene during amino acid deprivation can be rescued in Atf4-deficient cells by inhibition of deacetylation. *J. Biol. Chem.* **287**, 36393–36403 (2012).
58. Tameire, F. et al. ATF4 couples MYC-dependent translational activity to bioenergetic demands during tumour progression. *Nat. Cell Biol.* **21**, 889–899 (2019).
59. Zyryanova, A. F. et al. ISRIB blunts the integrated stress response by allosterically antagonising the inhibitory effect of phosphorylated eIF2 on eIF2B. *Mol. Cell* **81**, 88–103.e106 (2021).
60. Sidrauski, C. et al. Pharmacological brake-release of mRNA translation enhances cognitive memory. *Elife* **2**, e00498 (2013).
61. Chou, A. et al. Inhibition of the integrated stress response reverses cognitive deficits after traumatic brain injury. *Proc. Natl. Acad. Sci. USA* **114**, E6420–E6426 (2017).
62. Zyryanova, A. F. et al. Binding of ISRIB reveals a regulatory site in the nucleotide exchange factor eIF2B. *Science* **359**, 1533–1536 (2018).
63. Krukowski, K. et al. Small molecule cognitive enhancer reverses age-related memory decline in mice. *Elife* **9**, e62048 (2020).
64. Halliday, M. et al. Partial restoration of protein synthesis rates by the small molecule ISRIB prevents neurodegeneration without pancreatic toxicity. *Cell Death Dis.* **6**, e1672 (2015).
65. Barragan-Iglesias, P. et al. Activation of the integrated stress response in nociceptors drives methylglyoxal-induced pain. *Pain* **160**, 160–171 (2019).
66. Kabir, Z. D. et al. Rescue of impaired sociability and anxiety-like behavior in adult cacna1c-deficient mice by pharmacologically targeting eIF2 α . *Mol. Psychiatry* **22**, 1096–1109 (2017).
67. Watanabe, S. et al. Resetting proteostasis with ISRIB promotes epithelial differentiation to attenuate pulmonary fibrosis. *Proc. Natl. Acad. Sci. USA* **118**, e2101100118 (2021).
68. Cho, W. et al. A phase 1 first-in-human study to investigate the safety, tolerability and food effect of ABBV-CLS-7262 (P6-4.002). *Neurology* **100** (17 Supplement 2) (2023).
69. Mederacke, I., Dapito, D. H., Affo, S., Uchinami, H. & Schwabe, R. F. High-yield and high-purity isolation of hepatic stellate cells from normal and fibrotic mouse livers. *Nat. Protoc.* **10**, 305–315 (2015).
70. Krige, D. et al. CHR-2797: an antiproliferative aminopeptidase inhibitor that leads to amino acid deprivation in human leukemic cells. *Cancer Res.* **68**, 6669–6679 (2008).
71. Fleming, S. J. et al. Unsupervised removal of systematic background noise from droplet-based single-cell experiments using CellBender. *Nat. Methods* **20**, 1323–1335 (2023).
72. Wolock, S. L., Lopez, R. & Klein, A. M. Scrublet: Computational identification of cell doublets in single-cell transcriptomic data. *Cell Syst.* **8**, 281–291.e289 (2019).
73. Wolf, F. A., Angerer, P. & Theis, F. J. SCANPY: Large-scale single-cell gene expression data analysis. *Genome Biol.* **19**, 15 (2018).
74. Xu, C. et al. Probabilistic harmonization and annotation of single-cell transcriptomics data with deep generative models. *Mol. Syst. Biol.* **17**, e9620 (2021).
75. La Manno, G. et al. RNA velocity of single cells. *Nature* **560**, 494–498 (2018).
76. Bergen, V., Lange, M., Peidli, S., Wolf, F. A. & Theis, F. J. Generalizing RNA velocity to transient cell states through dynamical modeling. *Nat. Biotechnol.* **38**, 1408–1414 (2020).

Acknowledgements

We thank Dr. Robert Weinberg (Whitehead Institute for Biomedical Research) for kindly sharing the HMLE and HMLER cells. We thank Drs. Dong Fang (Zhejiang University) and Sherry Lee (Peking University) for helpful advice on the ChIP assay. We thank Dr. Zhijian Sun (K2 Oncology) for helpful discussion on the manuscript. We thank Biolyx for providing support for IHC analysis. Funding: This study was funded by grants from the Ministry of Science and Technology of the People's Republic of China (2020YFA0803300, Y.-X.F.), the National Natural Science Foundation of China (32270783, 82188102, Y.-X.F.; 32100949, J.Y.; 32300642, L.-X.Y.), and Welch Foundation (AU-2000-20220331, P.M.).

Author contributions

Experimental design: Y.-X.F. and L.-X.Y. Data collection: L.-X.Y., C.Q., S.L., X.-S. Y., P.M., D.-Y.Z., J.-S.Z., J.C., Y.W. and J.Y. Data analysis: L.-X.Y., C.Q., S.L., Y.-X.F., W.L., P.M., T.Y., J.-S.Z., Y.W., Y.J., X. M., and B.S. Manuscript writing: Y.-X.F., L.-X.Y., W.L., S.L., J.Y. Supervision: Y.-X.F.

Competing interests

The authors declare no competing interests.

Additional information

Supplementary information The online version contains supplementary material available at <https://doi.org/10.1038/s41467-024-55738-1>.

Correspondence and requests for materials should be addressed to Jia You, Wenbo Li or Yu-Xiong Feng.

Peer review information *Nature Communications* thanks Dongryeol Ryu and the other, anonymous, reviewer(s) for their contribution to the peer review of this work. A peer review file is available.

Reprints and permissions information is available at <http://www.nature.com/reprints>

Publisher's note Springer Nature remains neutral with regard to jurisdictional claims in published maps and institutional affiliations.

Open Access This article is licensed under a Creative Commons Attribution-NonCommercial-NoDerivatives 4.0 International License, which permits any non-commercial use, sharing, distribution and reproduction in any medium or format, as long as you give appropriate credit to the original author(s) and the source, provide a link to the Creative Commons licence, and indicate if you modified the licensed material. You do not have permission under this licence to share adapted material derived from this article or parts of it. The images or other third party material in this article are included in the article's Creative Commons licence, unless indicated otherwise in a credit line to the material. If material is not included in the article's Creative Commons licence and your intended use is not permitted by statutory regulation or exceeds the permitted use, you will need to obtain permission directly from the copyright holder. To view a copy of this licence, visit <http://creativecommons.org/licenses/by-nc-nd/4.0/>.

© The Author(s) 2025